Band structure engineering enabled low thermal conductivity in Al, Sn codoped ZnO nanosheets with high thermoelectric performance

Althaf. R†, Hyoung-Won Son, Takao Mori,* ** Anuradha M Ashok †*

†Functional materials Laboratory, PSG Institute of Advanced Studies, Coimbatore-641004, India

* International Center for Materials Nanoarchitectonics (WPI-MANA), National Institute for Materials Science (NIMS), Tsukuba, Ibaraki 305-0044, Japan.

** Graduate School of Pure and Applied Sciences, University of Tsukuba, 1-1-1 Tennodai, Tsukuba, Ibaraki, 305-8577, Japan

KEYWORDS. Zinc oxide, Band structure, Nanosheets, Fermi level, Dislocation, Thermal conductivity

ABSTRACT.

Band structure engineering is an effective way to improve the Seebeck coefficient without affecting the electrical conductivity. This study Al 3*s* state hybridized with Zn 4*s* state shifts the Fermi level inside the conduction band in Al, Sn codoped ZnO exposing its metallic behavior. Sn impurity creates large density of states near Fermi level leading to high Seebeck coefficient. In this material, in addition to scattering of low-frequency phonons by interfaces and of high-

frequency phonons by point defects, scattering of mid-frequency phonons by dense dislocations, localized at the grain boundaries, has been an effective strategy to reduce the lattice thermal conductivity. Dual doping creates low angle grain boundaries composed of dislocation arrays with a misorientation less than about 13.5°. These dislocation arrays along with lattice strain significantly reduce the thermal conductivity to 6.391 W $m^{-1}K^{-1}$ at room temperature in $Zn_{0.97}Al_{0.02}Sn_{0.01}O$. All these effects lead to a high figure of merit ZT of 0.61 at 997 K. A single leg thermoelement fabricated using $Zn_{0.97}Al_{0.02}Sn_{0.01}O$ shows an open circuit voltage of 122 mV with ΔT at 500K.

Introduction:

Thermoelectric (TE) materials are of paramount importance in the direct conversion of heat energy into electrical energy ((Please add applicative references here: L. E. Bell, Science 321, 1457 (2008), I. Petsagkourakis et al., Sci. Tech. Adv. Mater., 19, 836-862 (2018) DOI: 10.1080/14686996.2018.1530938, Phil. Trans. R. Soc. A.37720180450, (2019), H. Akinaga, Jpn. J. Appl. Phys., 59 (2020) 110201, N. Nandihalli et al., Nano Energy 78, 105186 (2020) doi: 10.1016/j.nanoen.2020.105186)). The performance of a material for this application is quantified by the thermoelectric figure of merit, $zT = S^2\sigma T/(\kappa_e+\kappa_l)$, where S is the Seebeck coefficient, σ is the electrical conductivity, κ_e is the electronic thermal conductivity, κ_l is the lattice thermal conductivity and T is the absolute temperature.[1] Majority of these parameters (S, σ, and κ_e, except κ_l) depend upon the charge carrier concentration n.[2] In order to improve the thermoelectric performance of a material, the most effective approach followed has been to increase the power factor (σS^2) by increasing Seebeck coefficient without significantly deteriorating electrical conductivity.[3]((Please add the review T. Mori, Small, 13, 1702013 (2017)) In addition to rather exotic principles such as utilizing magnetism [Vaney et al., Materials Today Phys., 9, 100090

(2019), Y. Zheng et al., Sci. Adv. 5, eaat9461 (2019), Materials Today Phys., 9, 100090 (2019), S. Hebert, R. Daou, A. Maignan, S. Das, A. Banerjee, C. Bourgès, N. Tsujii, T. Mori, "Thermoelectric materials taking advantage of spin entropy: lessons from chalcogenides and oxides", Science and Technology of Advanced Materials, 22:1, 583-596 (2021)], energy filtering [A. Shakouri et al., Mater. Res. Soc. Proc. 545, 449 (1999), A. Soni et al., Nano letters 2012, 12 (8), 4305-4310], band engineering strategies have been proven to be effective for decoupling these parameters to achieve enhancement in power factor[The 2 references you have in 3 + T. Mori, Small, 13, 1702013 (2017)+ Y. Pei et al., Nature 473, 66–69 (2011)]. This has been demonstrated in many thermoelectric materials, where the transporting bands can be engineered to be converged in energy resulting in an increase in σ without affecting S.[4] On the other hand, low thermal conductivity can be achieved through scattering of phonons by atomic scale point defects,[5] softening of phonons and bonding,[6]((please add: A. R. Muchtar, et al., "Physical insights on the lattice softening driven mid-temperature range thermoelectrics of Ti/Zr-inserted SnTe – an outlook beyond the horizons of conventional phonon scattering and excavation of Heikes' equation for estimating carrier properties", Advanced Energy Materials, 11, 2101122 (2021).)) nano-micropores,[7]((please add: Y. Shimasaki, et al., "Preparation of mesoporous nitrogen-doped titania comprising large crystallites with low thermal conductivity", Nanoscale Advances, 4, 2509 (2022).)) nanoscale endotaxial inclusions,[8] all scale hierarchical architectures,[9] nano/meso-architectures,[10] inherent lattice anharmonicity[11]((please add: N. Sato, et al., "Bonding Heterogeneity in Mixed-Anion Compounds Realizes Ultralow Lattice Thermal Conductivity", J. Mater. Chem. A, 9, 22660-22669 (2021).)), interstitial site doping [Z. Liu, et al., Joule, 5, 1196-1208 (2021), Nat. Commun. 13, 1120 (2022).], and utilizing layered grains[12].

ZnO is a promising *n*-type semiconductor with wide band gap (~3.3 eV) and large Seebeck coefficient (~-400 μV K^{-1}). However, it has low electrical conductivity because of the covalent character of Zn-O bond with small electronegativity difference between the individual elements. This leads to relatively large carrier mobility with low charge carrier concentration (below 10^{18} cm^{-3}). Simple wurtzite crystal structure with lighter Zn and O elements results in a thermal conductivity of 100 W $m^{-1}K^{-1}$ at room temperature.[13] Several attempts and strategies have been adopted in the past with varying degrees of success to reduce the thermal transport in ZnO based materials such as doping with homologous compounds like InO and GaO for nanoscale engineering by creating nano inclusions of planar defects[14], superstructuring[15], pores/voids,[16] nano-graining,[17] nanoprecipitates,[18] grain boundaries,[19] point defects,[20] *etc*. Highly dense grain boundaries and interfaces make nanostructured doped ZnO effective in scattering phonons.[21-24] Nano-structured ZnO bulks are limited by their inherently low mobility caused by the high density of grain boundaries and interfaces. At the same time in polycrystalline ZnO, intrinsic defects like zinc vacancies (V_{Zn}) and interstitial oxygens (O_i) are more likely to exist in the GBs of *n*-type ZnO ceramics as localized acceptor state. These acceptors attract charge carriers to create a depletion region around the GBs and then an energy potential barrier is formed, which impede the motion of the electrons.[25-27] Thus reduction in thermal conductivity through nanostructuring and Schottky barrier at the GBs substantially limits the independent optimization of the electrical and thermal transport properties blocking any further improvement of TE performance in ZnO.[28] Enhancement in electrical conductivity was attempted through increase in carrier concentration by introducing dopants like (Al, Ga, In) and increase in carrier mobility was attempted via adding MWCNT in ZnO and RGO, MWCNT in Al doped ZnO nanocomposites. However, RGO, MWCNT encapsulated Al doped ZnO sample would show lower *S* compared to undoped ZnO encapsulated

with RGO, MWCNT.[29-37] The reason for this reduction in Seebeck coefficient will be explained in later section. Recently, defect design of ZnO grain structure was proposed. The results showed that the three-dimensional stacking faults designed in the grains led to a large increase in the defect scattering to suppress κ_l. Meanwhile these defects in the grains showed little influence on the electrical conductivity.[20] Therefore, to simultaneously increase the electrical conductivity and decrease the lattice thermal conductivity, three pathways are proposed: (i) decreasing the amount of acceptor defects at the GBs to lower the Schottky barrier and increase the mobility (ii) addition of dopants like Al^{3+}, Sn^{4+} to substitute for Zn^{2+} site to increase the carrier concentration without deterioration of Seebeck coefficient (iii) forming multidimensional lattice defects to increase the phonon scattering in order to lower κ_l. Related to these strategies, thermoelectric studies on individual Sn and Al doped ZnO have previously been reported, showing high power factors of 7.5×10^{-4} W m^{-1} K^{-2} at 730 ^{o}C (1 at% Al-doped ZnO)[18] and 1.1×10^{-3} W m^{-1} K^{-2} at 730 ^{o}C (1 at% Sn-doped ZnO)[38-40].

Herein we report the increase in carrier mobility via control of grain boundary orientation angles in nanostructured ZnO ceramics. We observe that in Al doped ZnO Fermi level moves inside the conduction band bringing about semiconductor to metal transition behavior. In Sn doped ZnO, formation of impurity states near Fermi level leads to high Seebeck coefficient. Simultaneous reduction in thermal conductivity can be achieved via all scale hierarchal structure along with dislocation induced lattice strain. Therefore, as illustrated in this work, codoping ZnO with Al and Sn is an effective strategy to increase both electrical conductivity and Seebeck coefficient, and attain reduction in thermal conductivity giving remarkable enhancement in the figure of merit ZT of 0.61 at 997 K. The experimental observations are supported by using the first-principles density functional theory (DFT) calculations of the electronic structure of ZnO and Al, Sn codoped ZnO.

The simulated data corroborated the hybridization of Al 3*s* in Zn 4*s* state and Sn 5*s* state creating new impurity states near Fermi level.

Details about the experimental procedures, characterization methods and computational studies are given in the supplementary data S1.

RESULTS AND DISCUSSION

Phase analysis:

The room temperature XRD patterns of the as-sintered pellets of ZnO, $Zn_{0.98}Al_{0.02}O$, $Zn_{0.99}Sn_{0.01}O$, and $Zn_{0.98-x}Al_{0.02}Sn_xO$ (x=0.01, 0.02, 0.03) are shown in Figure 2. All the major peaks in the diffractograms of ZnO, can be indexed according to wurtzite-type structure with hexagonal unit cell (space group: *P6₃mc*; JCPDS no. 36-1451).[41] The cell dimensions and cell volumes deduced through Rietveld refinement are listed in Table S1 in section S2 of the supplementary data.

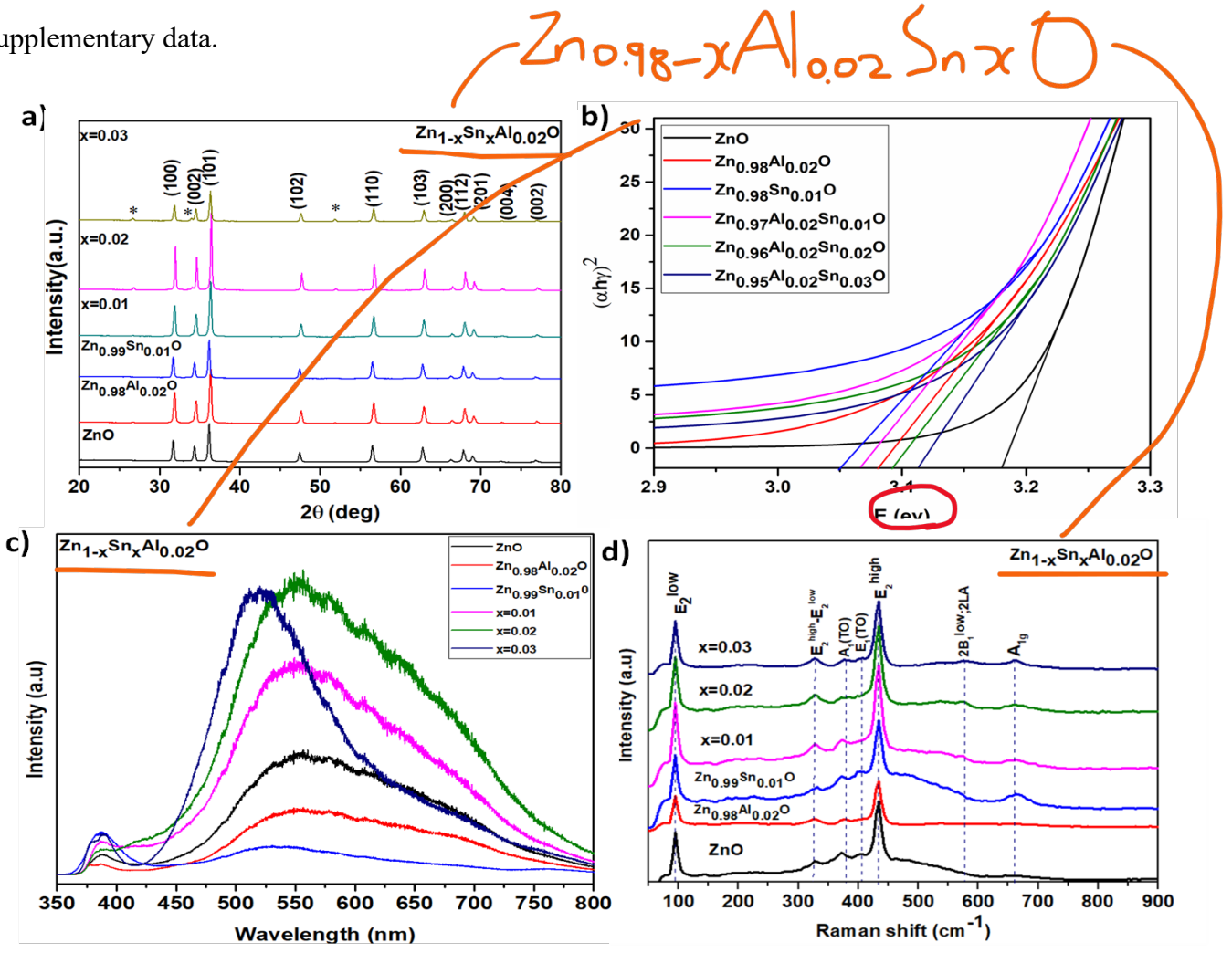

Figure 2. a) XRD patterns of sintered pellets b) Tauc plots c) PL spectra d) Raman spectra of ZnO, $Zn_{0.98}Al_{0.02}O$, $Zn_{0.99}Sn_{0.01}O$, and $Zn_{0.98-x}Al_{0.02}Sn_xO$ (x=0.01, 0.02, 0.03).

The XRD data of as-sintered samples $Zn_{0.98-x}Al_{0.02}Sn_xO$ (x=0.01, 0.02,0.03) reveal majority of wurtzite phase along with the minor diffraction peaks at 2θ= 26.6°, 33.5°and 51.9° (indicated by *) which is an additional superlattice peak, indicative of intergrowth or homologous phase formation. No additional phases corresponding to SnO, $ZnSnO_3$ or Zn_2SnO_4 are observed.[42,43] It can also be noted that diffractograms of some of Al, Sn codoped ZnO show higher peak intensity revealing their highly crystalline nature for compositions of ~~$Zn_{0.98}Sn_{0.02}O$,~~ $Zn_{0.98-x}Al_{0.02}Sn_xO$ (x=0.01, 0.02). For the composition with the highest Sn content (x=0.03) a reduction in peak intensity along with broadening indicates reduction in the crystallite size of the wurtzite phase.[38] Previous studies on Sn doped ZnO report that incorporation of Sn particularly restricts the growth along the c-axis of wurtzite ZnO.[39] 3% Sn concentration in $Zn_{0.98-x}Al_{0.02}Sn_xO$ could also have the effect of reducing or even destroying the crystallinity leading to amorphization of the ZnO structure.[47] Higher amount of Sn dopant can induce a large stress upon substitution for Zn/Al or incorporation in interstitial site, resulting in reduced crystallinity of $Zn_{0.98-x}Al_{0.02}Sn_xO$. However, in this study, a moderate effect, with minimal loss of crystallinity is observed.

Optical band gap studies:

Tauc plots of ZnO, $Zn_{0.98}Al_{0.02}O$, $Zn_{0.99}Sn_{0.01}O$, and $Zn_{0.98-x}Al_{0.02}Sn_xO$ (x=0.01, 0.02, 0.03) are shown in Figure 2 b). These plots were used to estimate optical band gaps. For pure/undoped ZnO, the observed band gap is 3.19 eV. Shift in the Tauc plots of the doped compositions towards the

left hand side of the energy axis reveals a decreasing trend in the band gap values with increase in dopant concentration. The observed narrowing of the band gap in Al, Sn codoped ZnO could be due to the increased hybridization of the energy levels in the O 2*p* orbitals, shifting the valence and conduction bands Al 3*s*, Sn 5*s* states towards lower values which is explained in DFT studies given in the later part of the manuscript. In the present case a red-shift can be observed due to merging of the impurity band into the conduction band, thereby shrinking the band gap from 3.19 eV to 3.05 eV. New impurity peaks formed near Fermi level cause band gap narrowing effect which is already reported in Sn doped ZnO systems.[44-49]

Photoluminescence (PL) studies:

Room temperature PL spectra of ZnO, $Zn_{0.98}Al_{0.02}O$, $Zn_{0.99}Sn_{0.01}O$, and $Zn_{0.98-x}Al_{0.02}Sn_xO$ (x=0.01, 0.02, 0.03) are presented in Figure 1(c). The near band edge (NBE) emission peaks from PL spectra of the donor element Al doped ZnO, Sn doped ZnO and Al, Sn codoped ZnO nanostructures exhibit a blue-shift in comparison to that observed for the undoped ZnO nanostructures. In the PL spectra of $Zn_{0.98}Al_{0.02}O$ and $Zn_{0.99}Sn_{0.01}O$, the intensity of the green band-edge emission is significantly suppressed. Herein, the intensity reduction is coupled with significant broadening because of the visible defect emission bands, which could be related to the reduced number of oxygen vacancies ($V_O^{\cdot\cdot}$) due to donor doping in ZnO. Nevertheless, several studies on the visible luminescence of ZnO and its origin are still controversial and a number of suggestions have been made.[26] The green luminescence has been attributed to defects such as oxygen vacancies and zinc vacancies as well as donor acceptor pairs.[26,46,49] The most striking observation of the photoluminescence data is that in the spectrum obtained for $Zn_{0.98-x}Al_{0.02}Sn_xO$ (x=0.01, 0.02, 0.03) the green band emission is effectively increased when compared to pure ZnO. This implies that with the simultaneous substitution of Al and Sn, intrinsic $V_O^{\cdot\cdot}$ defects are increased

in the samples. This evidence provides important insight into the role of Al, Sn addition to the ZnO matrix.[49] This observation also justifies the drastic increase in carrier concentration in Al, Sn codoped composition which is explained in later section. This result is also in line with XRD and Raman spectroscopy data, which shows the presence and influence of secondary phase in doped samples.

Raman Spectroscopy studies:

According to the group theory predictions ZnO crystals with hexagonal wurtzite structure and C_6v_4 symmetry have eight sets of phonon normal modes at the Γ point, represented as $\Gamma = 2A_1 + 2E_1 + 2B_1 + 2E_2$. Among them, one set of A_1 and E_1 modes is acoustic, while the remaining ones are optical modes. Both A_1 and E_1 are Raman and infrared active whereas E_2 is Raman active only and B_1 is inactive i.e. silent mode. Moreover, the A_1 and E_1 modes are polar and split into transverse optical (TO) and longitudinal optical (LO) components. The E_2 mode consists of two modes, of low and high frequency phonons (E_2^{low} and E_2^{high}), associated with the vibration of the heavy ZnO sublattice and oxygen atoms, respectively.[47,48] Room temperature Raman spectra of ZnO, $Zn_{0.98}Al_{0.02}O$, $Zn_{0.99}Sn_{0.01}O$, and $Zn_{0.98-x}Al_{0.02}Sn_xO$ (x=0.01,0.02,0.03) are shown in figure 2 d). The vibrational modes in the spectrum of ZnO are assigned as follows: An intensive peak near 100 cm^{-1} is ascribed to the vibrations of the zinc sublattice in ZnO.[49] The peaks at 330 cm^{-1}, 379 cm^{-1} and 405 cm^{-1} are due to the second-order vibration mode E_2^{high}–E_2^{low}, the transverse-optical mode A_1 (TO) and the transverse optical mode E_1 (TO), respectively. A sharp and intensive peak near 440 cm^{-1} is due to E_2^{high} mode which is related to vibration of oxygen attached to zinc atoms in the tetrahedral coordination.[49] The strong E_2^{high} mode indicates high crystallinity which is in good correlation with the XRD data. The peak at 590 cm^{-1} is attributed to A_1 (LO) and E_1 (LO) modes, while peak at 657 cm^{-1} represents combination of transverse acoustic and longitudinal

optical modes (TA + LO). These two peaks reveal the existence of lattice defects, in particular, oxygen vacancies and zinc interstitials.[50-52] The Raman spectrum of tin oxide shows the peaks centered at 474 cm^{-1}, 633cm^{-1}, and 776 cm^{-1} which are ascribed to the Eg, A_{1g}, and B_{2g} modes of SnO_2, respectively. [53]Due to high intensity of peaks of ZnO these peaks are suppressed.

Scanning electron microscopy analysis:

Figure 3 (a-i) show SEM micrographs of fracture surfaces of the sintered pellets of ZnO, $Zn_{0.98}Al_{0.02}O$, $Zn_{0.99}Sn_{0.01}O$ and $Zn_{0.98-x}Al_{0.02}Sn_xO$ (x=0.01, 0.02, 0.03). The fracture surface is parallel to the pressure axis which is applied while pelletisation. All micrographs clearly indicate hexagonal flake like morphology (micro/nanosheets) of ZnO. The micrographs of the $Zn_{0.98}Al_{0.02}O$ and $Zn_{0.99}Sn_{0.01}O$ pellets (Figure 2 (b) and (c)) reveal that the individual sheets are strongly inter-connected with one another. $Zn_{0.99}Sn_{0.01}O$ has much thinner micro/nanosheets when compared to $Zn_{0.98}Al_{0.02}O$ and $Zn_{0.98-x}Al_{0.02}Sn_xO$ (x=0.01, 0.02, 0.03) samples. $Zn_{0.98-x}Al_{0.02}Sn_xO$ (x=0.01) appears to be composed of strong connecting networks of micro/nanosheet arrays with grain size of 5 ~ 6 μm as shown in figure 2 (h) and (i). Though some specific arrangement of smaller nanosheets can be observed in $Zn_{0.98-x}Al_{0.02}Sn_xO$ (x=0.02) no such regular microstructure was observed in $Zn_{0.98-x}Al_{0.02}Sn_xO$ (x=0.03), as shown in figure 2 (e) and (f). This kind of mixed micro/nanosheet morphology scatters all frequency phonons without disturbing mobility of charge carriers resulted an overall improvement in thermoelectric performance compared with other different morphologies in doped ZnO.[54-62]

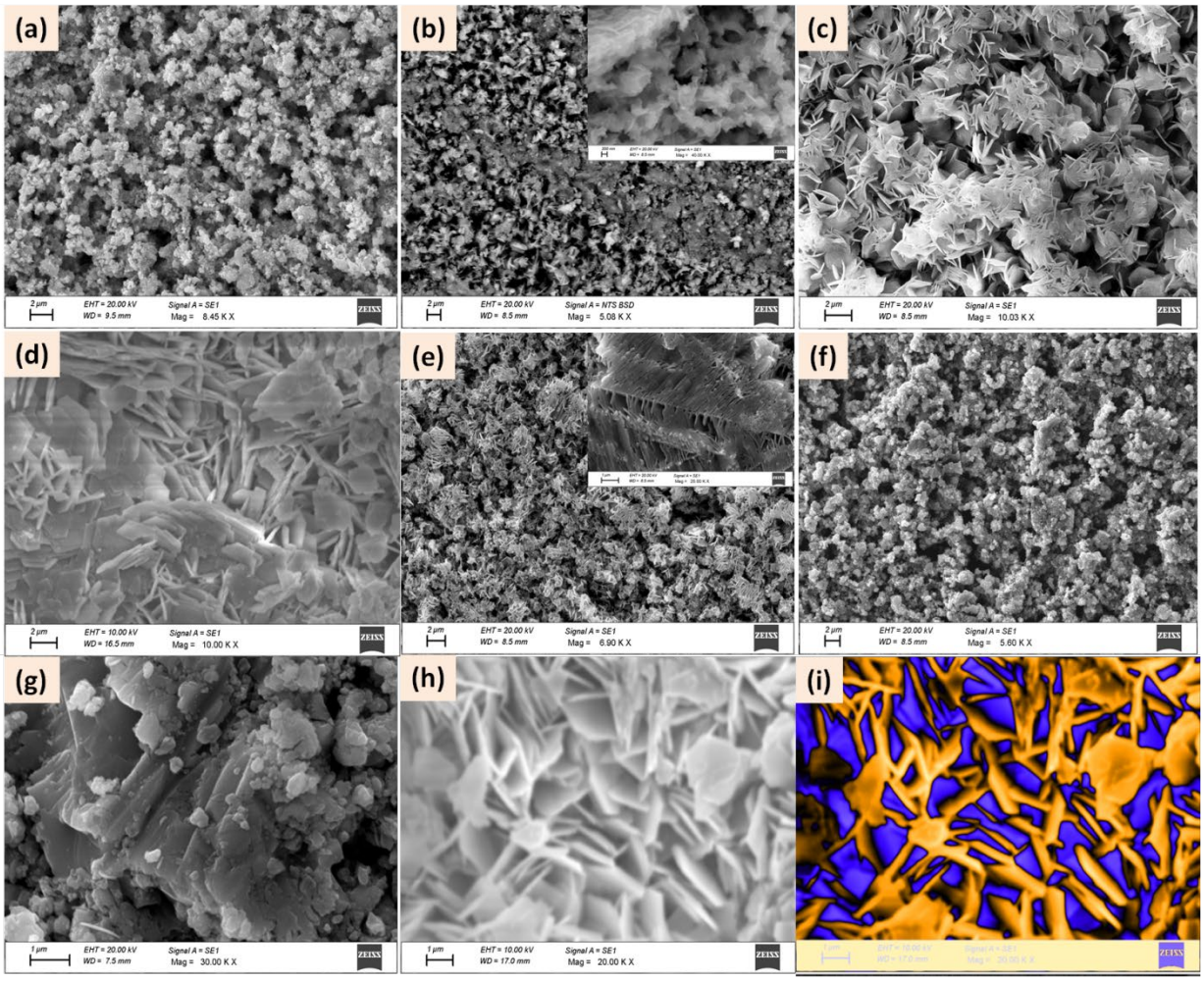

Figure 3. SEM micrographs of fracture surfaces of sintered pellets (a) ZnO (b) $Zn_{0.98}Al_{0.02}O$, (c)$Zn_{0.99}Sn_{0.01}O$, and (d), (e) and (f) $Zn_{0.98-x}Al_{0.02}Sn_xO$ (x=0.01, 0.02, 0.03). (g) enlarged top view of $Zn_{0.98-x}Al_{0.02}Sn_xO$ (x=0.01), (h) and (i) images of $Zn_{0.98-x}Al_{0.02}Sn_xO$ (x=0.01) depicting strong connecting networks of micro/nanosheets.

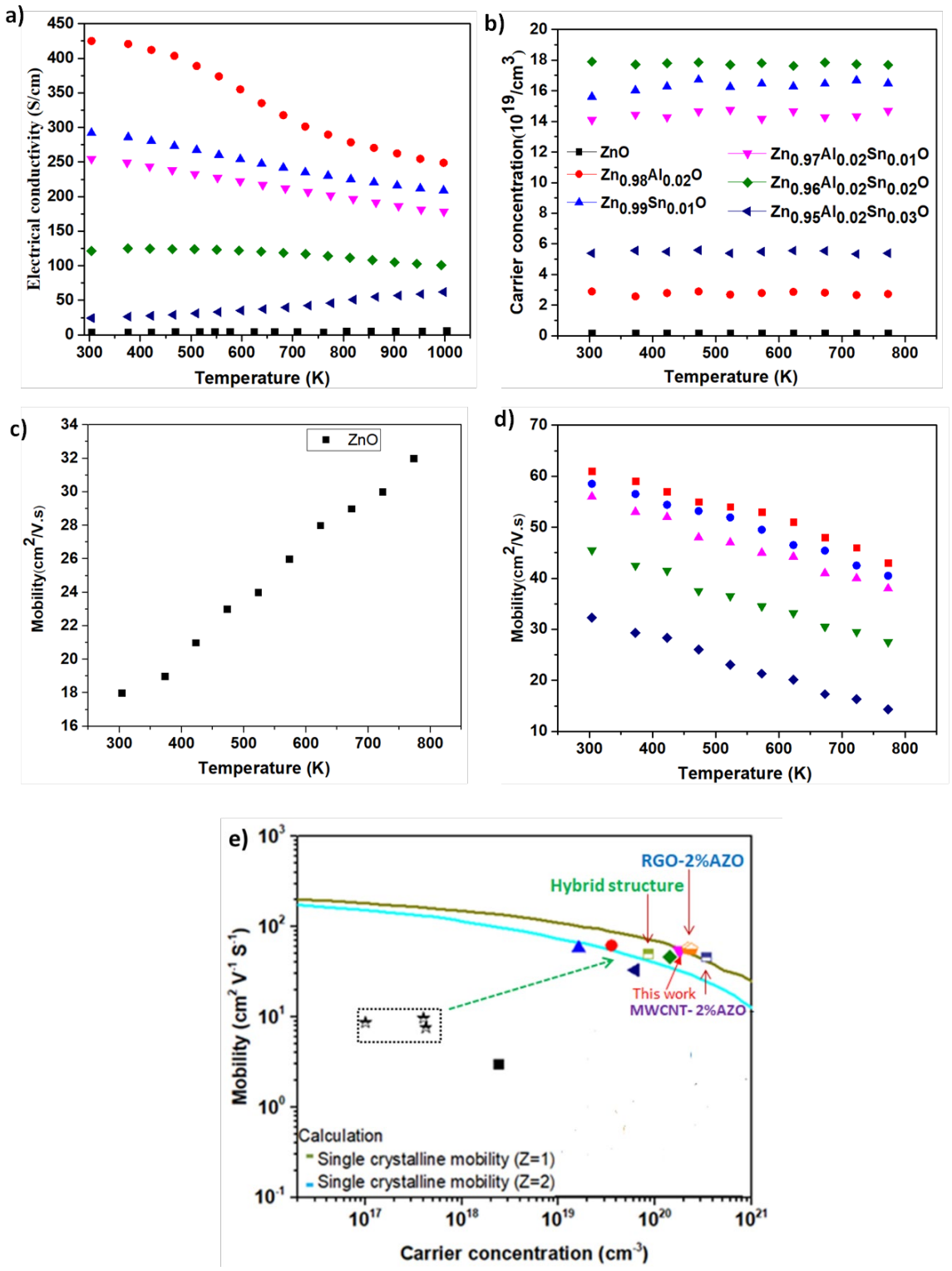

Figure 4. Temperature dependent of a) electrical conductivity, b) carrier concentration, c) charge carrier mobility of ZnO, d) charge carrier mobility of $Zn_{0.98}Al_{0.02}O$, $Zn_{0.98}Sn_{0.01}O$, and $Zn_{0.98-}$

$_{x}Sn_{x}Al_{0.02}O$ (x=0.01, 0.02, 0.03), and e) a comparison of the room temperature mobility as a function of carrier concentration values obtained in this work with the reported data. The star marks indicate the mobilities of undoped polycrystalline ZnO composites with different microstructures reported in the literatures. The dark olive and cyan curves are the calculated single crystalline mobilities of ZnO for Z = 1 and 2.

Thermoelectric properties:

Temperature dependent of electrical conductivity(s) of ZnO, $Zn_{0.98}Al_{0.02}O$, $Zn_{0.99}Sn_{0.01}O$, and $Zn_{(0.98-x)}Al_{0.02}Sn_{x}O$ (x=0.01, 0.02, 0.03) are presented in Fig. 4 a). A decrease in electrical conductivity with increase in temperature is observed in all Al, Sn codoped ZnO samples, which is the typical behaviour of degenerate semiconductors. An overall increment in electrical conductivity is observed when ZnO is doped with Al, and/or Sn. At room temperature, the observed electrical conductivity of ZnO is 3.8 S/cm. With the substitution of 2 % Al^{3+}, 1 % Sn^{4+} in Zn^{2+} sites, the room temperature electrical conductivity increases to 425 S/cm and 295 S/cm, respectively. In $Zn_{0.98-x}Al_{0.02}Sn_{x}O$ (x=0.01, 0.02, 0.03) electrical conductivity values at the room temperature are 255 S/cm, 121 S/cm and 24 S/cm, respectively. The replacement of Zn^{2+} with Sn^{4+} increases the free charge carrier concentration to compensate for the electrical charge balance which in turn improves the electrical conductivity of the sample. Higher Sn content in ZnO gives rise to the formation of additional superlattice peak in $Zn_{0.98-x}Sn_{x}Al_{0.02}O$ (x=0.02, 0.03), whose presence decreases the electrical conductivity in them. Addition of dopants cause an increase in carrier concentration which is shown in Fig. 4 b). Figure 4 c) and d) represent temperature dependent mobilities of undoped and doped ZnO, respectively. In undoped ZnO, grain boundary scattering significantly suppresses the mobility leading to the positive temperature-dependence in electrical conductivity for overcoming the Schottky barrier at the grain boundaries. However, the

electrical conductivities in $Zn_{0.98-x}Sn_xAl_{0.02}O$ (x=0.01, 0.02, 0.03) revealed the negative temperature-dependence as shown in Fig. 4 d), indicating that the effect of the grain boundary scattering could be negligible. The absence of grain boundary scattering is proven through calculations. (The details of calculations are shown in Section S4. of the supporting information). Fig. 4 e) gives the room temperature mobility as a function of carrier concentration of the compositions studied in this work in comparison with the reported values in literature.[37, 63-65.] The room temperature mobility of undoped ZnO prepared in this study is compared with that of undoped polycrystalline ZnO composites with different microstructures (indicated by star marks in the plot) reported in literature.[40-42] Dark olive and cyan curves are the calculated single crystalline mobilities of ZnO for Z = 1 and 2. If electrons in undoped ZnO are provided dominantly by the intrinsic point defects like oxygen vacancies and/or zinc interstitials, Z becomes 2 since the electrons are scattered mostly by V_O^{2+} and/or Zn_i^{2+}. However, when most of electrons are donated by extrinsic dopant, like in the case of Al and Sn doped ZnO, Z becomes 1 due to the ionized impurity scattering by singly charged positive ions of Al^{3+}, Sn^{4+}.[35, 37.] The room temperature mobilities of $Zn_{0.98}Al_{0.02}O$ and $Zn_{0.99}Sn_{0.01}O$ are closer to the calculated single crystalline mobility for Z = 2, demonstrating that majority of the electrons are scattered by doubly charged ionized impurity. However, $Zn_{0.98-x}Al_{0.02}Sn_xO$ (x=0.01) exhibited single crystalline mobility for Z = 1, which is determined by the singly ionized impurity ions, indicating that most of the electron conduction was carried out through ZnO possessing Al and Sn ions. These results demonstrate that the enhanced charge transport is mainly induced by the simultaneous increase in the carrier concentration and the mobility through the release of the trapped electrons from the grain boundaries. A significant improvement in the mobility also could be realized by the bulk ZnO

made up of micro/nano sheets with very small misorientation angles between the grains due to the alleviated grain boundary scattering as discussed in later section.

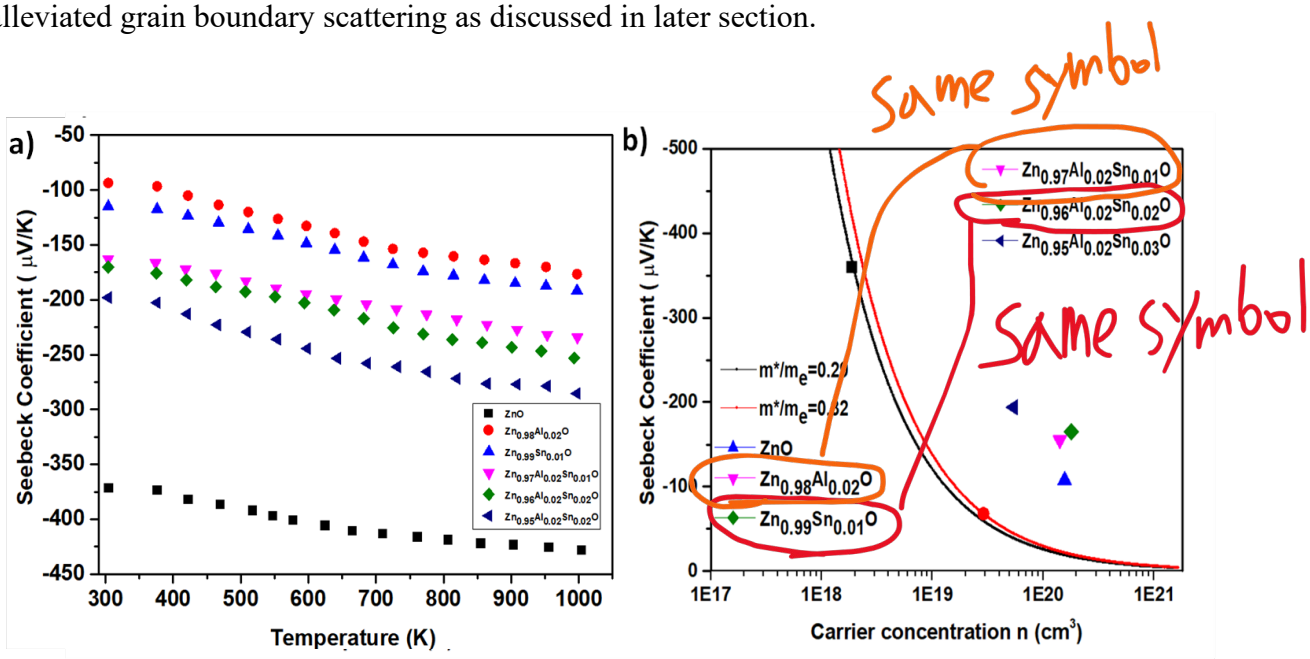

Figure 5. Temperature dependent a) Seebeck coefficient and b) Pisarenko curve of ZnO, $Zn_{0.998}Al_{0.02}O$, $Zn_{0.99}Sn_{0.01}O$, $Zn_{(0.98-x)}Sn_xAl_{0.02}O$ (x=0.01,0.02,0.03).

As shown in Fig. 5 a), temperature dependent Seebeck coefficients of all compositions are negative indicating n-type conduction. The Seebeck coefficient of the undoped ZnO sample at the room temperature (303 K) is about -371 μV K^{-1} due to its low intrinsic carrier concentration. Seebeck coefficients of $Zn_{0.98}Al_{0.02}O$ and $Zn_{0.99}Sn_{0.01}O$ are about -94 μV K^{-1} and -115 μV K^{-1} at 303 K which increase up to -177 μV K^{-1} and -192 μV K^{-1} at 1002 K, respectively. Interestingly, for Al, Sn co-doped samples, a synergistic increase in Seebeck coefficient value can be observed when compared to those of individual Al and Sn doped samples over the whole temperature range. The Seebeck coefficient values of $Zn_{0.98-x}Al_{0.02}Sn_xO$ for x=0.01, 0.02 and 0.03 are -163μV K^{-1}, -170μV K^{-1}, and -198 μV K^{-1} at 303 K which increases up to -234 μV K^{-1}, -253 μV K^{-1} and -285 μV K^{-1} at 1002 K. In general, the value of the Seebeck coefficient in common semiconductors decreases with

an increase in carrier concentration. In this case, the Seebeck coefficient values of different compositions are in congruence with their respective carrier concentration. However, the observed temperature dependence of both the electrical conductivity and the Seebeck coefficient in Sn doped and Al, Sn codoped samples is unusual. Similar behavior has been previously observed in Sn and Al, Sn codoped Samples. To understand this unusual behavior, as a first step the effective mass is calculated using the Single Parabolic Band (SPB) model.[56] According to Pisarenko relation for degenerate semiconductors, the expression for Seebeck coefficient is given by

$$S = \frac{8\pi^2 k_B^2 T}{3qh^2} m^* \left(\frac{\pi}{3n}\right)^{2/3} \quad \text{.....(1)}$$

where k_B is the Boltzmann constant, T is the absolute temperature, h is Planck's constant, q is the electron charge, and m^* is the DOS effective mass at the Fermi level. By plotting the room temperature S versus $n^{2/3}$ the m^* of the ZnO can be estimated to be 0.29 m_e. According to the measured n and estimated m^* values, a SPB model can be generated by employing the following equations[16]:

$$F_r = \int_0^\infty \frac{x^r}{1+\exp(x-\xi)} dx \quad \text{.....(2)}$$

$$n = \frac{4}{\pi}\left(\frac{2\pi m^* k_B T}{h^2}\right)^{3/2} F_{1/2} \quad \text{.....(3)}$$

$$S = -\frac{k_B}{e}\left[\frac{\left(\frac{5}{2}+\lambda\right)F_{3/2+\lambda}}{\left(\frac{3}{2}+\lambda\right)F_{1/2+\lambda}} - \xi\right] \quad \text{.....(4)}$$

Where F_r is the Fermi integral and ξ is the reduced electrochemical potential. λ is the scattering parameter, which is assumed to be 0 for acoustic phonon scattering, 1 for optical phonon scattering, and 2 for ionized impurity scattering. The calculated effective masses m^* of ZnO, $Zn_{0.98}Al_{0.02}O$, $Zn_{0.99}Sn_{0.01}O$, and $Zn_{0.98-x}Al_{0.02}Sn_xO$ (x=0.01, 0.02, 0.03) samples with acoustic phonon scattering

mechanism (λ=0) are 0.42, 0.32, 0.72, 0.53 and 0.47, respectively. Sn doped and Al, Sn codoped samples show higher Seebeck coefficient than the Pisarenko line of ZnO curve as shown in figure 5 b) due to their increased density of states. To understand the origin of the enhanced Seebeck coefficient the electronic structure calculations of undoped, Al doped, Sn doped and Al, Sn codoped ZnO were performed, which will be discussed in later section. From the band structure and density of states calculations, it can be observed that upon addition of single dopants like Al or Sn in ZnO, Fermi level moves deeper inside the conduction band causing increase in charge carrier concentration supporting the enhancement in electrical conductivity. Due to the shifting of Fermi level deeper into conduction band, the absolute value of Seebeck coefficient at the room temperature becomes substantially low (~100 $\mu V\ K^{-1}$) compared to pure ZnO (350 $\mu V\ K^{-1}$).[20] In Al, Sn codoped ZnO, the presence of Al brings the Fermi level near to conduction band minimum and due to Sn, extended density of states are formed with stronger hybridization which causes increased effective mass leading to increase in Seebeck coefficient which is shown in schematic Fig. 13. By using this strategy a moderate electrical conductivity with high Seebeck coefficient can be maintained. Position of the Fermi level is important in order to estimate Seebeck coefficient. We have calculated the position of Fermi level for doped ZnO in existing literature with respect to reported Seebeck coefficient, carrier concentration and effective mass, which are shown in table 1.[18,31,35,36,54,56,61] In RGO/ZnO nanocomposite the Fermi level lies deep inside the conduction band and no significant change in effective mass is observed. This is also one of the reasons for the reduction of Seebeck coefficient.

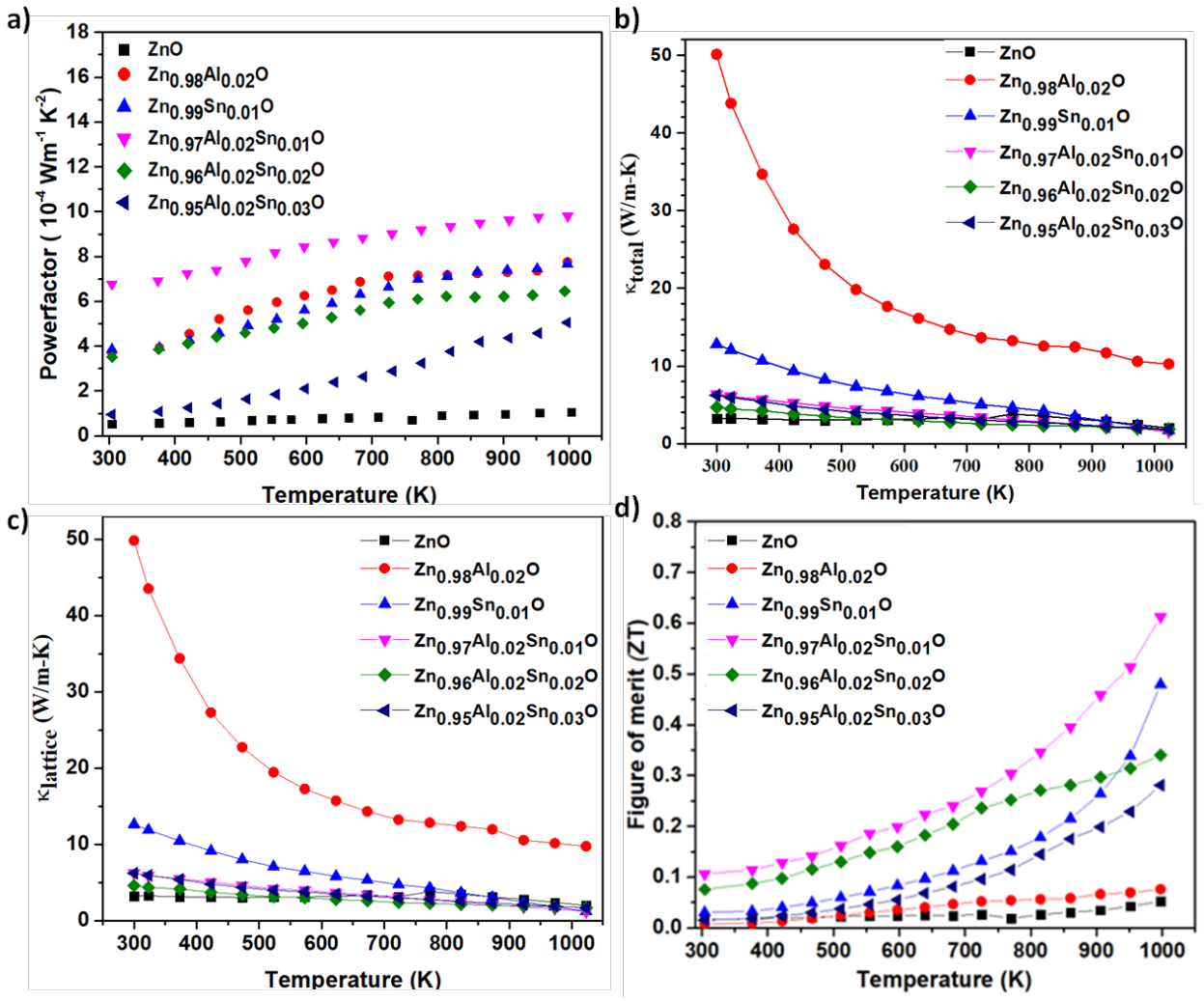

Figure 6. a) Temperature dependent power factors, b) total thermal conductivity, c) lattice thermal conductivity, and d) figure of merit ZT of ZnO, $Zn_{0.98}Al_{0.02}O$, $Zn_{0.99}Sn_{0.01}O$, $Zn_{0.98-x}Al_{0.02}Sn_xO$ (x=0.01, 0.02, 0.03) samples.

Figure 6 a) represents the temperature dependent power factors of ZnO, $Zn_{0.98}Al_{0.02}O$, $Zn_{0.99}Sn_{0.01}O$, $Zn_{0.98-x}Sn_xAl_{0.02}O$ (x=0.01, 0.02, 0.03) samples. $Zn_{0.98-x}Al_{0.02}Sn_xO$ (x=0.01) shows the highest power factor value over a wide range of temperature from 6.76 $\times 10^{-4}$ W $m^{-1}K^{-2}$ at 303K, increasing up to 9.80 $\times 10^{-4}$ W $m^{-1}K^{-2}$ at 1002 K due to its high Seebeck coefficient and optimal electrical conductivity compared to individual Al or Sn doped ZnO. $Zn_{0.98}Al_{0.02}O$ and $Zn_{0.99}Sn_{0.01}O$

samples show 3.73 $\times 10^{-4}$ W $m^{-1}K^{-2}$ and 3.86 $\times 10^{-4}$ W $m^{-1}K^{-2}$ at 303 K, increasing up to 7.76 $\times 10^{-4}$ W $m^{-1}K^{-2}$ and 7.67 $\times 10^{-4}$ W $m^{-1}K^{-2}$ at 997 K, respectively. Figure 6 b) represents the temperature dependent thermal conductivities of ZnO, $Zn_{0.98}Al_{0.02}O$, $Zn_{0.99}Sn_{0.01}O$, $Zn_{0.98-x}Al_{0.02}Sn_xO$ (x=0.01, 0.02, 0.03) samples. A decrease in thermal conductivity with increase in temperature can be observed in all the samples. Micro/Nanostructured pellets of ZnO exhibit a thermal conductivity value of 3.214 $Wm^{-1}K^{-1}$ at 300 K which is much lower than that of non-nanostructured ZnO.[55-57] To best of our knowledge this is the lowest thermal conductivity of undoped ZnO reported so far. When doped with Al, the thermal conductivity of ZnO increases to 50.1 W $m^{-1}K^{-1}$ at 300 K which is mainly due to larger micrograin networks as revealed by TEM images shown in S2. $Zn_{0.99}Sn_{0.01}O$ and $Zn_{0.98-x}Al_{0.02}Sn_xO$ (x=0.01, 0.02, 0.03) show thermal conductivity values of 12.7 W $m^{-1}K^{-1}$, 6.3 W $m^{-1}K^{-1}$, 4.6 W $m^{-1}K^{-1}$ and 6.2 W $m^{-1}K^{-1}$ at 300 K, respectively. The thermal conductivity values of the Al, Sn codoped compositions of ZnO are higher than those reported in literature.[32] The lattice contribution κ_L to the κ_{total} was estimated using the reduced Lorenz number of 1.8×10^{-8} $W\Omega K^{-2}$.[35] The extracted κ_L values are shown in Fig. 6 (c). The values of κ_L are similar to the values of κ_{total}, indicating that the lattice component dominates the thermal conductivity in all the samples. Multidimensional lattice defects (including 2D grain boundaries, 2D nanostructure interfaces, 1D dislocations, and 0D point defects) due to Al, Sn codoping evidently account for κ_L-reduction behavior in the present work.[64-74] Further, phonon transport by different scattering mechanisms including Umklapp-process (Um), point defect (PD), grain boundaries (GB), and dislocations (DS) were calculated and compared with experimental κ_L of $Zn_{0.97}Al_{0.02}Sn_{0.01}O$ (Fig. 7 a)). The spectral lattice thermal conductivity (κ_s) with respect to the phonon frequency (ω) was determined using the modified Debye Callaway model (Fig. 7 b))[66,69,72] (The details of phonon transport calculations and values are shown in Section S5. of the supporting information). It is

noticeable that the Umklapp-process and electrons (the cyan area) can scatter phonons in whole frequency range and grain boundaries (the yellow area) can effectively scatter low-frequency phonons, while the middle- and high-frequency phonons are scattered by point defect and dislocations (the green area). From this observation reduction of κ_L in ZnO based systems could be achieved via controlling i) grain size ii) pore size and iii) adding dopants which effectively scatter high- and low-frequency phonons compared to middle-frequency phonons.[21,17,28] Jood et al., reported that $ZnAl_2O_4$ nano precipitates in ZnO nanocomposite reduce thermal conductivity ~ 3 W $m^{-1}K^{-1}$ at 300 K by scattering mid- and high-frequency phonons.[18] It is clearly evident that, low κ_L in $Zn_{0.97}Al_{0.02}Sn_{0.01}O$ comes from scattering of full spectrum phonons by misorientation between grain boundaries, dislocations and point defects without deteriorating electrical conductivity.

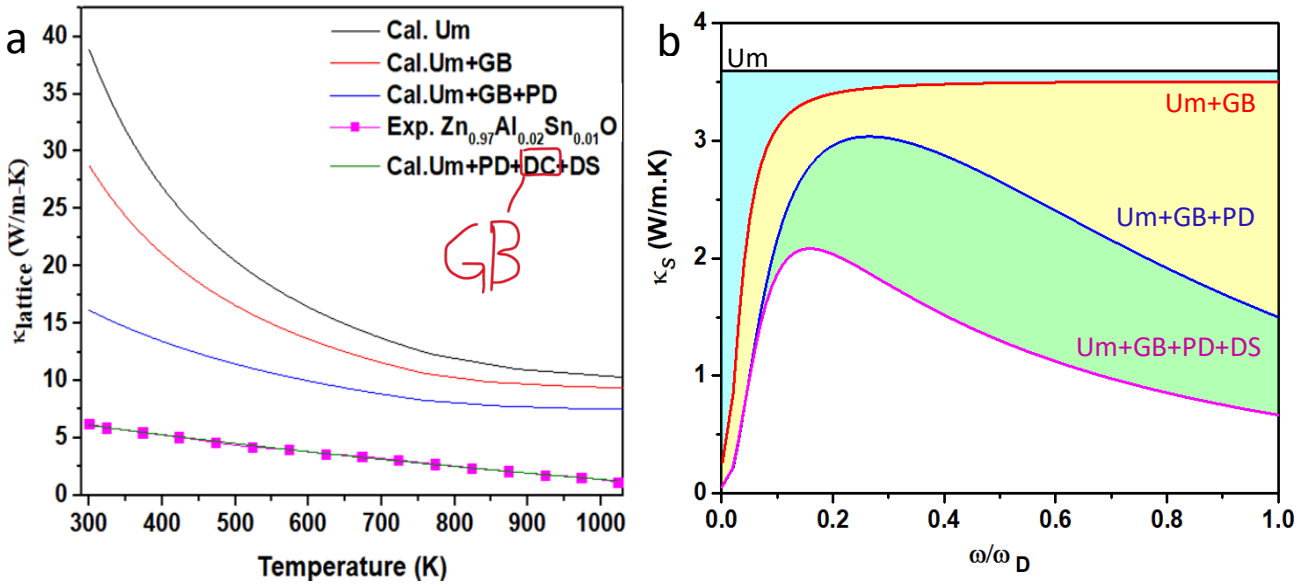

Figure 7. a) Comparison of experimental data and calculated lattice thermal conductivity of $Zn_{0.97}Al_{0.02}Sn_{0.01}O$ the solid lines represent the calculated κ_L when phonon scattering from three phonon Umklapp processes (Um), grain boundaries (GB), point defects (PD), and Dislocations (DS) and **b)** Calculated contribution of different phonon scattering mechanisms to the spectral

lattice thermal conductivity (κ_s) using Debye-Callway model with various phonon scattering mechanisms including (U), (GB), (PD), and (DS) at 300 K.

Temperature dependent figure of merit (ZT) of ZnO, $Zn_{0.98}Al_{0.02}O$, $Zn_{0.99}Sn_{0.01}O$, $Zn_{0.98-x}Al_{0.02}Sn_xO$ (x=0.01, 0.02, 0.03) samples are shown in Fig. 6 d). Despite having the lowest thermal conductivity, undoped ZnO shows the lowest ZT value of 0.05249 at 1002 K due to its lowest power factor. Because of its highest thermal conductivity value, $Zn_{0.98}Al_{0.02}O$ show low ZT values in the range of 0.07606 and ~~0.47~~ between 303 K and 997 K. Sn doped ZnO exhibits moderate value of 0.47 at 997 K compared with the existing reports on the same composition.[38] However, $Zn_{0.97}Al_{0.02}Sn_{0.01}O$ exhibits the highest ZT value of 0.61 at 997 K. To best of our knowledge this is the highest ZT being reported for codoped ZnO. ZT values of 0.33 and 0.28 exhibited by $Zn_{1-x}Al_{0.02}Sn_xO$ (x=0.02, 0.03) show the effectiveness of codoping in improvement of thermoelectric properties of ZnO when compared to single element doping. The higher ZT values of Al, Sn codoped ZnO when compared to singly doped ZnO is due to the enhancement in power factor and reduction in thermal conductivity.

In order to elucidate the reasons for such a low lattice thermal conductivity of $Zn_{0.97}Al_{0.02}Sn_{0.01}O$ and $Zn_{0.96}Al_{0.02}Sn_{0.02}O$ samples, extensive microscopy study was conducted by Transmission Electron Microscopy (TEM).

Transmission Electron Microscopy analysis of $Zn_{0.98-x}Al_{0.02}Sn_xO$ (x=0.01) pellet:

The electron transport properties and low thermal conductivity of $Zn_{0.97}Al_{0.02}Sn_{0.01}O$ were further corroborated with TEM analysis.

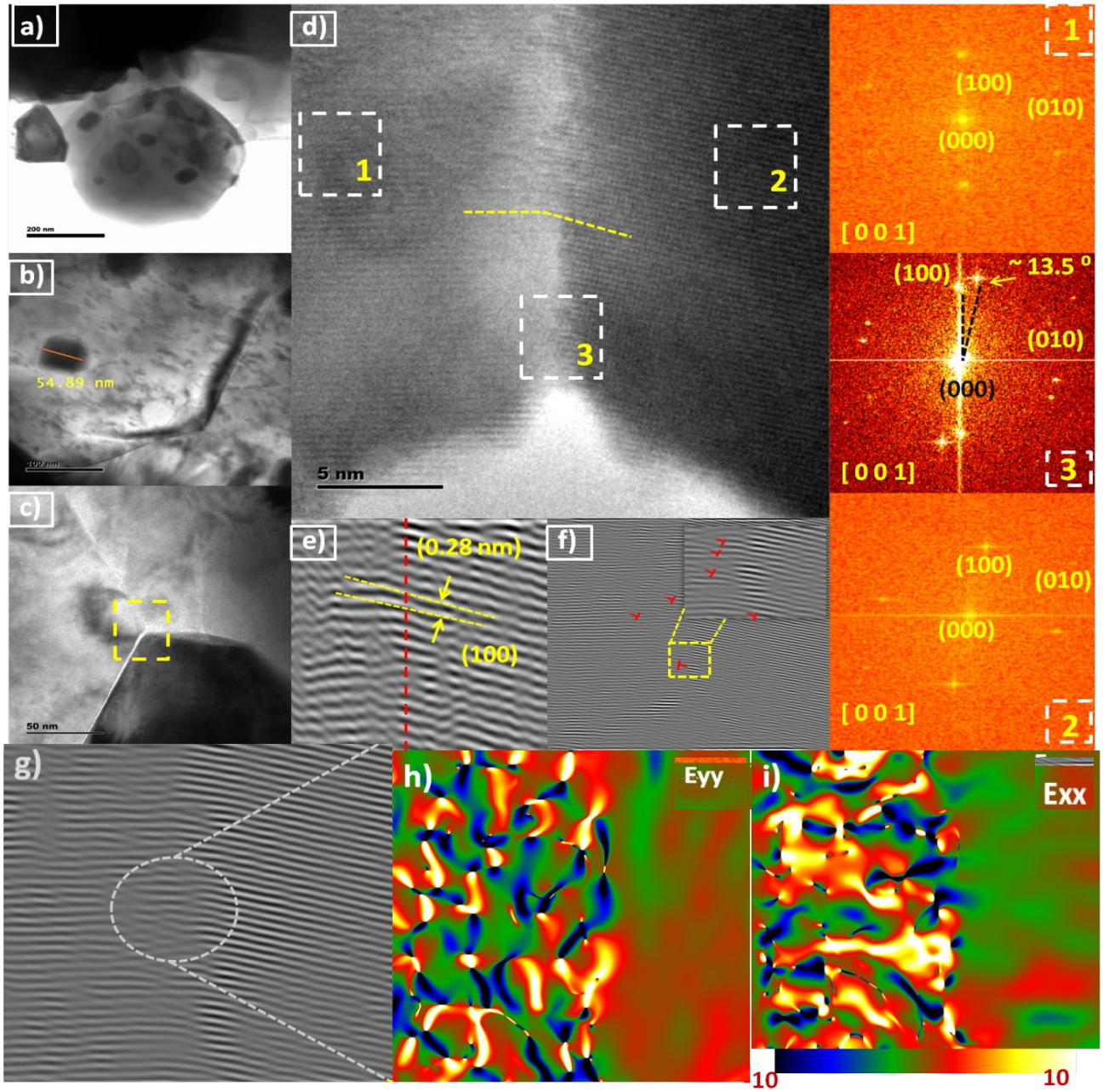

Figure 9. a) TEM image of sintered pellet, b) mixed micro-nano sheets, c) at the interconnection of three micro-nano sheets, d) enlarged HRTEM image and corresponding FFT ED patterns of selected regions marked 1, 2 and 3 on the image of the sintered pellet. e) mis-orientation between the two grains and *d* spacing of 0.28 nm (100 plane). f) and g) enlarged HRTEM image with dislocations of $Zn_{0.97}Al_{0.02}Sn_{0.01}O$ (x=0.01). h) and i) geometric phase analysis of $Zn_{0.97}Al_{0.02}Sn_{0.01}O$ (x=0.01).

In order to get an insight of the grain boundary structure and misorientation degree among the oriented micro/nanograins, HRTEM and Fast Fourier Transformation Electron Diffraction (FFT ED) analyses were performed. Figures 9 a), b) and c) affirm that the bulk pellet of

$Zn_{0.97}Al_{0.02}Sn_{0.01}O$ is comprised of micro/nano sheets. Figure 9 d) depicts the high resolution image taken at the interface between two micro sheets. According to the FFT diffractograms acquired from the regions 1, 2 and 3 marked within dashed white squares, each micro-nanograin exhibits a nearly identical ED pattern along [001] zone-axis. An interplanar spacing of 0.28 nm corresponding to the distance between the (100) planes of ZnO also can be observed in both the regions (Fig. 9 e)).[80] The presence of uniform fringes even across the grain boundaries (region 3) can be observed as shown from the HRTEM images. The FFT ED pattern obtained from region 3 shows a combination of the ED patterns corresponding to both the grains oriented at an angle of ~13.5º.[78] This reveals a ~13.5º mis-orientation between the (100) planes across two adjacent grains. The inversed FFT image of region 3 also reveals the existence of several periodic edge dislocations arrays along the grain boundary (marked in red) as shown in Fig. 9 f), which play a major role in the electron and phonon transport. Geometric phase analysis (GPA) is a semi-quantitative lattice image-processing approach for the evaluation of spatially distributed strain fields by combining the real space and reciprocal space information. Displacements measured by calculating local Fourier components in Fig. g) can be mapped in Fig. h) and i). Large dislocations may meet and interact within an individual grain leading to the formation of low angle grain boundary.[85,79] GPA analysis confirms the strain fluctuation induced by lattice dislocations. In Fig. h) and i) ε_{yy} and ε_{xx} components of the strain, reveal isotropous feature of the strain. Since dense dislocations are converging as strip-like shapes at nanoscale (the strip-like defects), an extra high density of dislocations can be realised. These randomly distributed dislocations combined with the accumulated local strain contribute to strong scattering for both high-frequency and mid-frequency phonons, and thus an increase in lattice strain causes reduction in lattice thermal conductivity.[86-88] The above structural analysis also demonstrates the formation of typical ~~nanoscale~~ mosaic

micro/nanostructure in polycrystalline grains in $Zn_{0.97}Al_{0.02}Sn_{0.01}O$. This novel mixed micro and nano grains are different from the conventional nanocrystals or nanocomposite materials in which nanograins are randomly oriented with misaligned interfaces which would strongly affect electron transfer. This characteristic feature is consistent with the mosaic structure obtained in $Cu_2(S, Te)$ polycrystalline bulks.[62] Similar effect is observed in Al doped ZnO samples in which nanograins are oriented randomly. Their misaligned interfaces affect electron transfer by grain boundary scattering and impurity defect scattering.[75-77] Additionally, the micro/nano grains in the sheets exhibited single crystalline nature with specific and ordered orientation along the axial direction (Figure 9). The tiny misorientaion in between the individual grains provides independent pathways for electrons and phonons. To conclude, electron transfer occurs along nearly coherent crystalline framework while phonons are blocked frequently by the strained lattices containing the dense network of dislocation edges.[86] The presence of mixed micro/nanosheets facilitate synergistic optimisation of both electrical and thermal transport properties. As a result, the material will behave like a crystal from the perspective of electron while the phonon will make it function as glassy material. As depicted in Fig. 9, through the fabrication of bulk sample comprising micro/nano sheets, the classic thermoelectric concept of "phonon-glass electron-crystal" characteristics are achieved[37].

Room temperature thermal conductivity of $Zn_{0.96}Al_{0.02}Sn_{0.02}O$ was found to be lower compared to $Zn_{0.97}Al_{0.02}Sn_{0.01}O$. It originates mainly from the formation of inter domain boundaries (IDB).[89] In the present case two effects can be observed: (i) Dopants with higher valences such as Sn^{4+} do not induce ID network formation; instead, the addition of these dopants to ZnO results in the formation a microstructure with a single basal-IDB (b-IDB) in each grain. (ii) Dopants such as Al^{3+} which have not been found to stabilize IDB development in ZnO, cause only spinel phase formation.

When ZnO is doped with either Sn or Al individually, ID network formation does not occur even after long sintering times at high temperatures-conditions favorable for ID network formation.[42,83] However, as shown in Fig. 10 a), ID networks do form in $Zn_{0.97}Al_{0.02}Sn_{0.01}O$, indicating the importance of Sn, Al co-doping for their formation and stabilization. Thus, considering the low solubility limits of Al and Sn in ZnO (Al: 0.3 at. %, Sn: < 0.1 at. %), [39,43] the formation of ID networks appears to be stabilized in $Zn_{0.96}Al_{0.02}Sn_{0.02}O$ in order to facilitate the inclusion of excess Sn and Al at the respective sites of the b-IDBs and pyramidal -IDBs. Moreover, the formation of the $ZnAl_2O_4$ and Zn_2SnO_4 spinel phases, which form in ZnO doped with either Al or Sn, was suppressed in Sn-Al dual-doped ZnO. This is attributed to the formation of stable inversion domain networks, consisting of Sn-rich octahedral basal-plane and Al-rich five-fold pyramidal-plane IDB sites, which avoid the unfavorable co-occupation of the spinel octahedral site by the significantly size-mismatched Sn and Al dopants.[42,83,84,90,91]. Along with the IDBs the presence of stacking faults help in reducing the thermal conductivity in Al, Sn codoped samples when compared to single element doped ZnO.

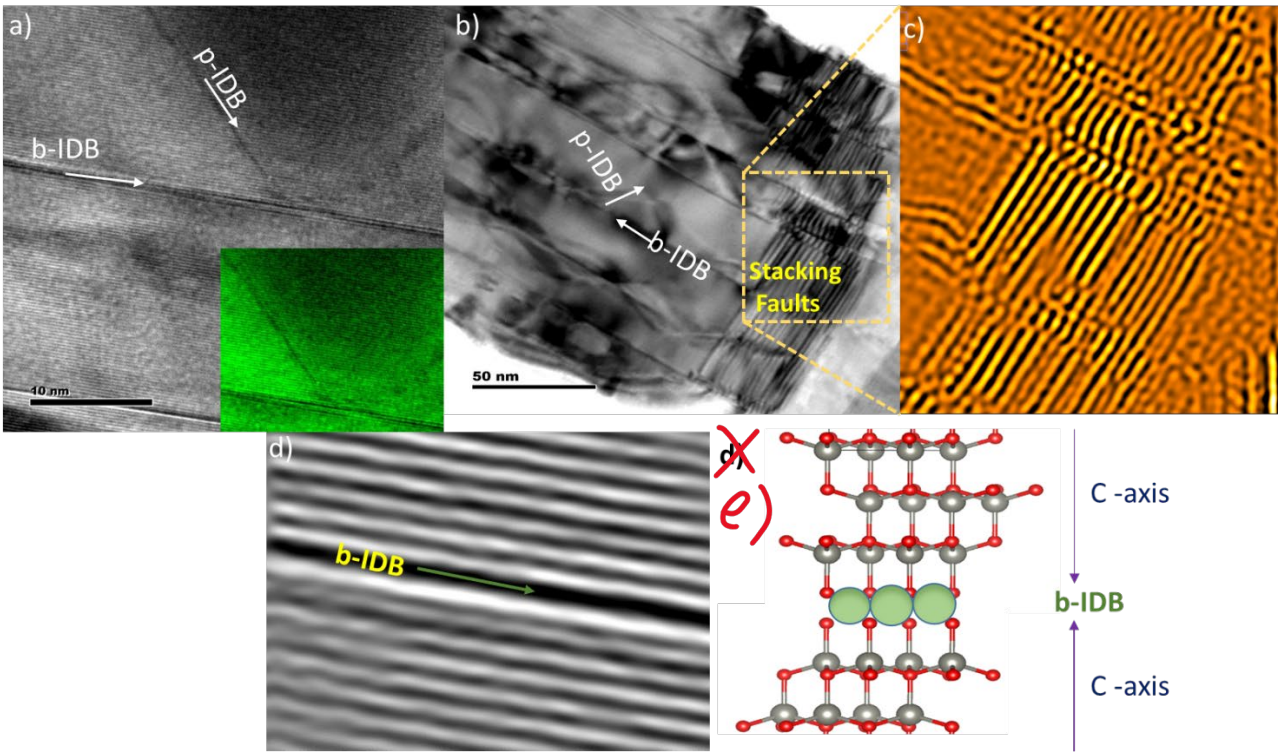

Figure 10. a) TEM image of $Zn_{0.96}Al_{0.02}Sn_{0.02}O$ pellet with b-IDBs and p-IDBs, b) large grain with b-IDBs, p-IDBs and stacking faults, c) filtered enlarged stacking faults, d) lattice fringes of $Zn_{0.96}Al_{0.02}Sn_{0.02}O$ and e) schematic representation of b-IDBs in ZnO.

To test its efficacy, a single leg thermo-element $Zn_{0.97}Al_{0.02}Sn_{0.01}O$ was fabricated. The details of the fabrication are given in the supplementary information and shown in Figure S2 (1.7). The open circuit voltage measured with cold side at 300 K, and hot side at 373 K, 474 K, 573 K, 673 K, 773 K are shown in Fig. 11. The maximum open circuit voltage of 122 mV was observed with the ΔT 500 K.

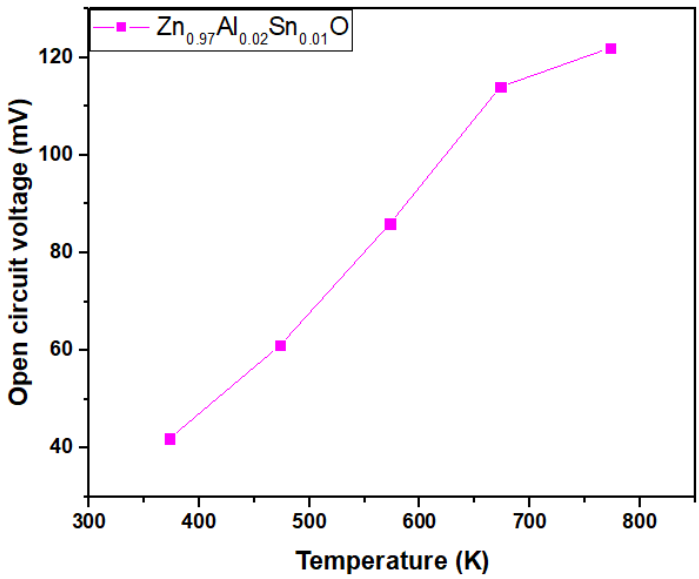

Figure 11. Temperature dependent open circuit voltage with cold side maintained at 300 K.

Computational details:

Simulated Band structures of ZnO, $Zn_{0.97}Al_{0.03}O$, $Zn_{0.97}Sn_{0.03}O$ and $Zn_{0.94}Al_{0.03}Sn_{0.03}O$ are shown in Fig. 12.

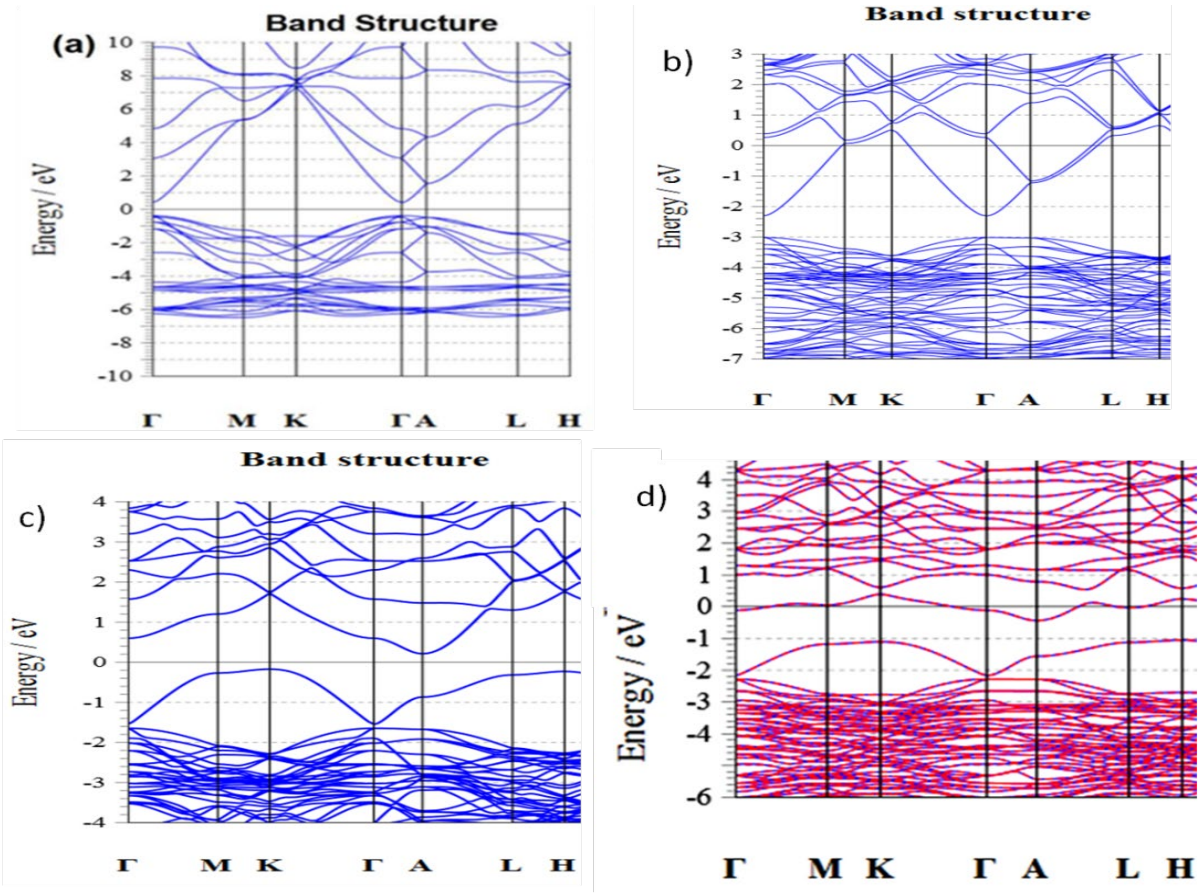

Figure 12. Band structures of a) ZnO, b) $Zn_{0.97}Al_{0.03}O$, c) $Zn_{0.97}Sn_{0.03}O$ and d) $Zn_{0.94}Al_{0.03}Sn_{0.03}O$.

The valence band maxima (VBM) and conduction band minima (CBM) at Γ point for all samples are indicating that ZnO is a direct band gap semiconductor. In Fig. 12 b) the Fermi level of Al doped ZnO lies within the conduction band. Introduction of Sn atoms into ZnO can change its band structure distinctly by moving the Fermi level substantially within the conduction band. In Fig. 12 c) and d) the band structure of Sn doped ZnO and Al, Sn codoped ZnO show significant modification in the form of stronger band split appearing near the Fermi level. Theoretical band gap values were calculated from the band structures. The band gap of pure ZnO is well below the experimentally obtained value of 3.4 eV.[34] This could be due to the underestimation for the band gap by CGA (comprehensive genetic algorithm).[98]

Simulated density of states of ZnO, $Zn_{0.97}Al_{0.03}O$, $Zn_{0.97}Sn_{0.03}O$ and $Zn_{0.94}Al_{0.03}Sn_{0.03}O$ are shown in Fig. 12.

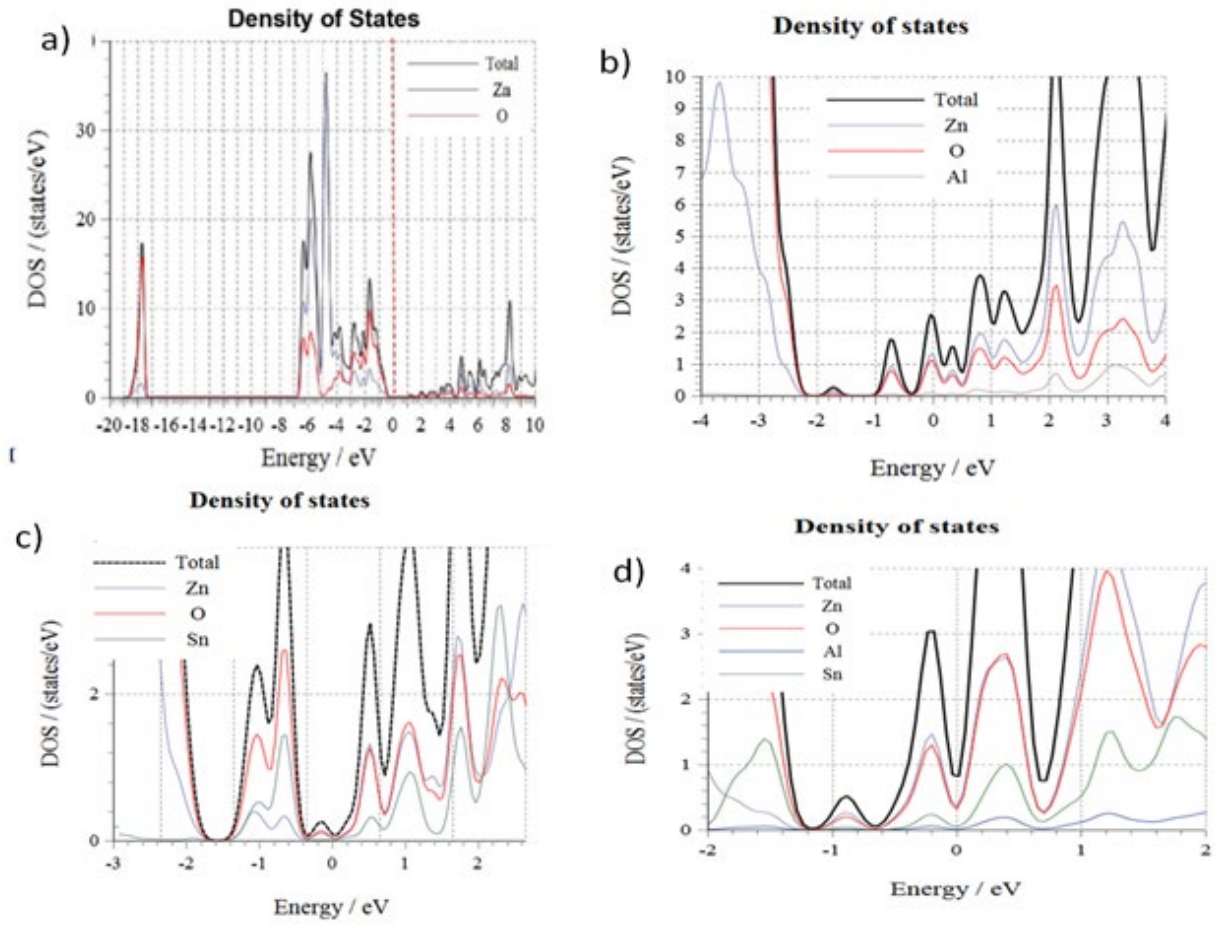

Figure 12. Density of states of a) ZnO, b) $Zn_{0.97}Al_{0.03}O$, c) $Zn_{0.97}Sn_{0.03}O$ and d) $Zn_{0.94}Al_{0.03}Sn_{0.03}O$.

The valence band consists of two regions, the lower valence band between -9 and -5 eV and the upper valence band between -5 and -2 eV. The lower valence band is contributed by the Zn 3d states, the upper valence band is from O 2p states and the bottom of the conduction band is dominated by Zn 4s and O 2s states which are shown in Fig. 12 a). In Fig. 12 b) and c) the upward shift of O 2p states in valence band and downward shift of Al 3s, Zn 4s states in conduction band cause reduction in the band gap of Al doped ZnO and Sn doped ZnO. Band gap reduction originates from the enhancement of p-d coupling in ZnO. Additionally, the new unoccupied DOS caused by strong *s–p* hybridization of Al-O, Sn-O bonds is incorporated into the conduction band. Impurity peak formed near the Fermi level is favorable for the improvement in conductivity of ZnO. The upper conduction band within -0.96 to 0 eV is mainly contributed by Sn -5s states near the Fermi level. The lower conduction band is constituted by Sn-p and Zn-s states. The valence band consists of two parts: the upper valence band within -19 to -18 eV introduced by O-s state, and the lower

valence band within -8.71 to -8.31 eV introduced by Zn-d state. Schematic representation of position of Fermi level in ZnO, $Zn_{0.98}Al_{0.02}O$, $Zn_{0.99}Sn_{0.01}O$, $Zn_{0.97}Sn_{0.01}Al_{0.02}O$ are shown in Fig. 13.

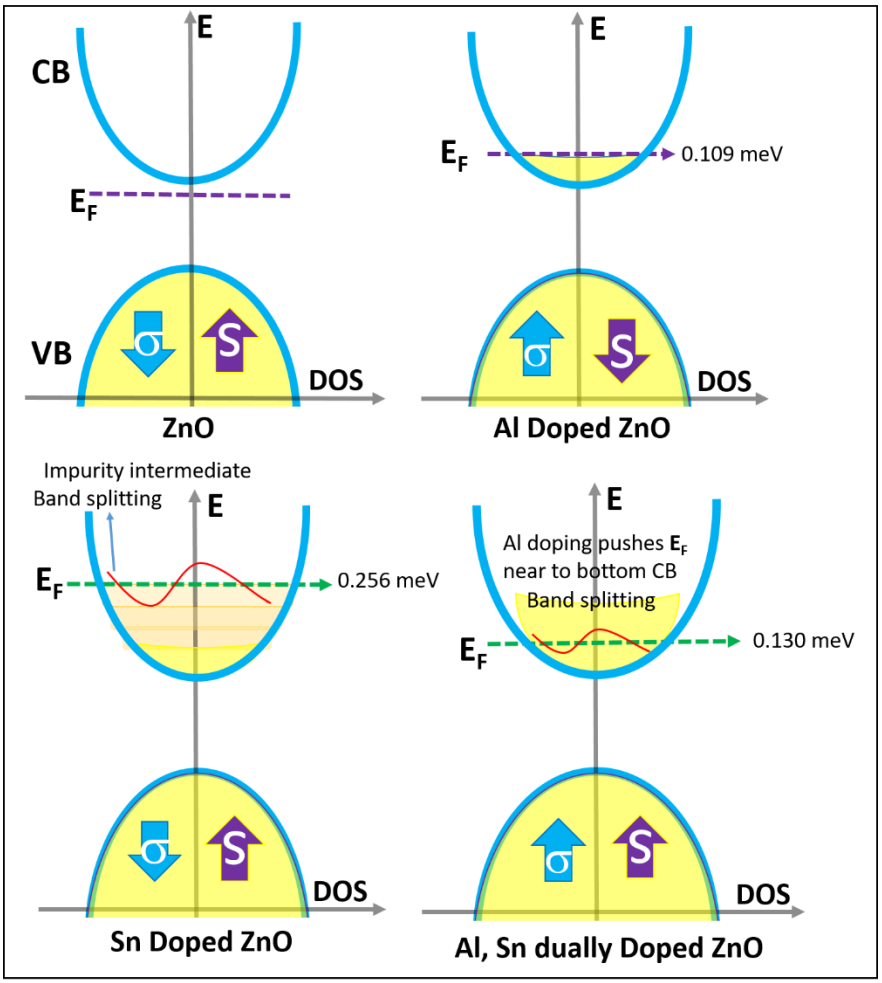

Figure 13. Schematic representation of the position of the Fermi level in ZnO, $Zn_{0.98}Al_{0.02}O$, $Zn_{0.99}Sn_{0.01}O$ and $Zn_{0.97}Al_{0.02}Sn_{0.01}O$.

Conclusion:

ZnO, $Zn_{0.98}Al_{0.02}O$, $Zn_{0.99}Sn_{0.01}O$, $Zn_{0.98-x}Al_{0.02}Sn_xO$ (x=0.01, 0.02, 0.03) samples were synthesized by sol-gel method. $Zn_{0.99}Sn_{0.01}O$ and Al, Sn codoped ZnO samples exhibit a high Seebeck coefficient over a wide temperature range due to the conduction band splitting near Fermi level, as confirmed with DFT calculations of the electronic structure. Nevertheless, they exhibit moderate electrical conductivity when compared with $Zn_{0.98}Al_{0.02}O$. A remarkably low thermal conductivity of micro nanostructured ZnO of 3.214 W $m^{-1}K^{-1}$ at 303 K is achieved, which is the lowest among the undoped nanostructured ZnO reported so far. Among the studied compositions

the highest ZT 0.61 at 997 K was recorded for $Zn_{0.98-x}Al_{0.02}Sn_xO$ (x=0.01) sample. The results observed in this study suggest that thermal conductivity of ZnO can be effectively reduced without adding any dopants by micro nanostructuring along with introducing dislocations. $Zn_{0.98-x}Al_{0.02}Sn_xO$ (x=0.01) is an important candidate for mid temperature thermoelectric power generation.

ACKNOWLEDGMENT

Author AR wish to acknowledge UGC-Moulana Azad National Fellowship financial support. This work is funded by DST-SERB (EMR/2016/006430). TM and HS acknowledge support from JST Mirai Program Grant Number JPMJMI19A1.

REFERENCES

1. Shi, X. L.; Zou, J.; Chen, Z. G. Advanced Thermoelectric Design: From Materials and Structures to Devices. *Chem. Rev.* **2020**, *120* (15), 7399–7515. https://doi.org/10.1021/acs.chemrev.0c00026.
2. Snyder, G. J.; Toberer, E. S. Complex Thermoelectric Materials. *Mater. Sustain. Energy A Collect. Peer-Reviewed Res. Rev. Artic. from Nat. Publ. Gr.* **2010**, *7* (February), 101–110. https://doi.org/10.1142/9789814317665_0016.
3. a)Qian, X.; Zhou, J.; Chen, G. Phonon-Engineered Extreme Thermal Conductivity Materials. *Nat. Mater.* **2021**, *20* (9), 1188–1202. https://doi.org/10.1038/s41563-021-00918-3.b) Muraleedharan, S.; Davis, N.; Althaf, R.; Singh, A.; Ashok, A. M. Exploring the Thermoelectric Behavior of Intrinsic and Defect Induced LaCoO3 with Selected Alkaline Earth Metals. *J. Alloys Compd.* **2021**, *857*, 157507. https://doi.org/10.1016/j.jallcom.2020.157507.
4. Qin, B.; Wang, D.; Zhao, L. D. Slowing down the Heat in Thermoelectrics. *InfoMat* **2021**, *3* (7), 755–789. https://doi.org/10.1002/inf2.12217.
5. Hu, L.; Zhu, T.; Liu, X.; Zhao, X. Point Defect Engineering of High-Performance Bismuth-Telluride-Based Thermoelectric Materials. *Adv. Funct. Mater.* **2014**, *24* (33), 5211–5218. https://doi.org/10.1002/adfm.201400474.
6. Hanus, R.; Agne, M. T.; Rettie, A. J. E.; Chen, Z.; Tan, G.; Chung, D. Y.; Kanatzidis, M. G.; Pei, Y.; Voorhees, P. W.; Snyder, G. J. Lattice Softening Significantly Reduces Thermal Conductivity and Leads to High Thermoelectric Efficiency. *Adv. Mater.* **2019**, *31* (21), 1–10. https://doi.org/10.1002/adma.201900108.
7. Khan, A. U.; Kobayashi, K.; Tang, D. M.; Yamauchi, Y.; Hasegawa, K.; Mitome, M.; Xue, Y.; Jiang, B.; Tsuchiya, K.; Golberg, D.; Bando, Y.; Mori, T. Nano-Micro-Porous Skutterudites with 100% Enhancement in ZT for High Performance Thermoelectricity. *Nano Energy* **2017**, *31*, 152–159. https://doi.org/10.1016/j.nanoen.2016.11.016.
8. Biswas, K.; He, J.; Zhang, Q.; Wang, G.; Uher, C.; Dravid, V. P.; Kanatzidis, M. G. Strained Endotaxial Nanostructures with High Thermoelectric Figure of Merit. *Nat. Chem.* **2011**, *3* (2), 160–166. https://doi.org/10.1038/nchem.955.

9. Biswas, K.; He, J.; Blum, I. D.; Wu, C. I.; Hogan, T. P.; Seidman, D. N.; Dravid, V. P.; Kanatzidis, M. G. High-Performance Bulk Thermoelectrics with All-Scale Hierarchical Architectures. *Nature* **2012**, *489* (7416), 414–418. https://doi.org/10.1038/nature11439.
10. Yang, G.; Niu, R.; Sang, L.; Liao, X.; Mitchell, D. R. G.; Ye, N.; Pei, J.; Li, J. F.; Wang, X. Ultra-High Thermoelectric Performance in Bulk BiSbTe/Amorphous Boron Composites with Nano-Defect Architectures. *Adv. Energy Mater.* **2020**, *10* (41), 1–8. https://doi.org/10.1002/aenm.202000757.
11. Wu, H.; Lu, X.; Wang, G.; Peng, K.; Zhang, B.; Chen, Y.; Gong, X.; Tang, X.; Zhang, X.; Feng, Z.; Han, G.; Zhang, Y.; Zhou, X. Strong Lattice Anharmonicity Securing Intrinsically Low Lattice Thermal Conductivity and High Performance Thermoelectric SnSb2Te4 via Se Alloying. *Nano Energy* **2020**, *76*. https://doi.org/10.1016/j.nanoen.2020.105084.
12. Alsalama, M. M.; Hamoudi, H.; Abdala, A.; Ghouri, Z. K.; Youssef, K. M. Enhancement of Thermoelectric Properties of Layered Chalcogenide Materials. *Rev. Adv. Mater. Sci.* **2020**, *59* (1), 371–378. https://doi.org/10.1515/rams-2020-0023.
13. Ohtaki, M. Oxide Thermoelectric Materials for Heat-to-Electricity Direct Energy Conversion. *Kyushu Univ. Glob. COE Progr. Nov. Carbon Resour. Sci. Newsl.* **2010**, *3* (January), 8.
14. Pham, A. T. T.; Luu, T. A.; Pham, N. K.; Ta, H. K. T.; Nguyen, T. H.; Van Hoang, D.; Lai, H. T.; Tran, V. C.; Park, J. H.; Lee, J. K.; Park, S.; Michitaka, O.; Park, S. D.; Nguyen, H. Q.; Phan, T. B. Multi-Scale Defects in ZnO Thermoelectric Ceramic Materials Co-Doped with In and Ga. *Ceram. Int.* **2020**, *46* (8), 10748–10758. https://doi.org/10.1016/j.ceramint.2020.01.084
15. Mohammed, M. A.; Sudin, I.; Noor, A. M.; Rajoo, S.; Uday, M. B.; Obayes, N. H.; Omar, M. F. A Review of Thermoelectric ZnO Nanostructured Ceramics for Energy Recovery. *Int. J. Eng. Technol.* **2018**, *7* (2), 27–30. https://doi.org/10.14419/ijet.v7i2.29.13120.
16. Virtudazo, R. V. R.; Guo, Q.; Wu, R.; Takei, T.; Mori, T. An Alternative, Faster and Simpler Method for the Formation of Hierarchically Porous ZnO Particles and Their Thermoelectric Performance. *RSC Adv.* **2017**, *7* (51), 31960–31968. https://doi.org/10.1039/c7ra05067d
17. a)Virtudazo, R. V. R.; Srinivasan, B.; Guo, Q.; Wu, R.; Takei, T.; Shimasaki, Y.; Wada, H.; Kuroda, K.; Bernik, S.; Mori, T. Improvement in the Thermoelectric Properties of Porous Networked Al-Doped ZnO Nanostructured Materials Synthesized: Via an Alternative Interfacial Reaction and Low-Pressure SPS Processing. *Inorg. Chem. Front.* **2020**, *7* (21), 4118–4132. https://doi.org/10.1039/d0qi00888e.b) Liu, S.; Li, G.; Lan, M.; Zhu, M.; Mori, T.; Wang, Q. Improvement of Thermoelectric Properties of Evaporated ZnO:Al Films by CNT and Au Nanocomposites. *J. Phys. Chem. C* **2020**, *124* (23), 12713–12722. https://doi.org/10.1021/acs.jpcc.0c01311.
18. Jood, P.; Mehta, R. J.; Zhang, Y.; Peleckis, G.; Wang, X.; Siegel, R. W.; Borca-Tasciuc, T.; Dou, S. X.; Ramanath, G. Al-Doped Zinc Oxide Nanocomposites with Enhanced Thermoelectric Properties. *Nano Lett.* **2011**, *11* (10), 4337–4342. https://doi.org/10.1021/nl202439h
19. Kim, K.; Park, J.; Hong, S.; Park, S. H.; Jeon, S. G.; Ahn, C.; Song, J. Y.; Jeon, S. Anomalous Thermoelectricity of Pure ZnO from 3D Continuous Ultrathin Nanoshell Structures. *Nanoscale* **2018**, *10* (6), 3046–3052. https://doi.org/10.1039/c7nr08167g.
20. Takemoto, H.; Fugane, K.; Yan, P.; Drennan, J.; Saito, M.; Mori, T.; Yamamura, H.

Reduction of Thermal Conductivity in Dually Doped ZnO by Design of Three-Dimensional Stacking Faults. *RSC Adv.* **2014**, *4* (6), 2661–2672. https://doi.org/10.1039/c3ra44223c.

21. Sulaiman, S.; Izman, S.; Uday, M. B.; Omar, M. F. Review on Grain Size Effects on Thermal Conductivity in ZnO Thermoelectric Materials. *RSC Adv.* **2022**, *12* (9), 5428–5438. https://doi.org/10.1039/d1ra06133j.
22. Zhao, Y.; Yan, Y.; Kumar, A.; Wang, H.; Porter, W. D.; Priya, S. Thermal Conductivity of Self-Assembled Nano-Structured ZnO Bulk Ceramics. *J. Appl. Phys.* **2012**, *112* (3). https://doi.org/10.1063/1.4745034
23. Kinemuchi, Y.; Nakano, H.; Mikami, M.; Kobayashi, K.; Watari, K.; Hotta, Y. Enhanced Boundary-Scattering of Electrons and Phonons in Nanograined Zinc Oxide. *J. Appl. Phys.* **2010**, *108* (5), 1–6. https://doi.org/10.1063/1.3475650.
24. Zakharchuk, K. V.; Widenmeyer, M.; Alikin, D. O.; Xie, W.; Populoh, S.; Mikhalev, S. M.; Tselev, A.; Frade, J. R.; Weidenkaff, A.; Kovalevsky, A. V. A Self-Forming Nanocomposite Concept for ZnO-Based Thermoelectrics. *J. Mater. Chem. A* **2018**, *6* (27), 13386–13396. https://doi.org/10.1039/c8ta01463a.
25. Look, D. C.; Droubay, T. C.; Chambers, S. A. Stable Highly Conductive ZnO via Reduction of Zn Vacancies. *Appl. Phys. Lett.* **2012**, *101* (10), 1–4. https://doi.org/10.1063/1.4748869.
26. McCluskey, M. D.; Jokela, S. J. Defects in ZnO. *J. Appl. Phys.* **2009**, *106* (7). https://doi.org/10.1063/1.3216464.
27. Tian, T.; Cheng, L.; Zheng, L.; Xing, J.; Gu, H.; Bernik, S.; Zeng, H.; Ruan, W.; Zhao, K.; Li, G. Defect Engineering for a Markedly Increased Electrical Conductivity and Power Factor in Doped ZnO Ceramic. *Acta Mater.* **2016**, *119*, 136–144. https://doi.org/10.1016/j.actamat.2016.08.026.
28. Ohtaki, M., Araki, K., & Yamamoto, K. (2009). High thermoelectric performance of dually doped ZnO ceramics. *Journal of Electronic Materials*, *38*(7), 1234-1238.
29. Trinh, T. Q.; Nguyen, T. T.; Vu, D. V.; Le, D. H. Microstructural Analysis and Thermoelectric Performance of Ga-Doped ZnO/Reduced Graphene Oxide Thin Film Nanocomposites. *Ceram. Int.* **2021**, *47* (22), 32033–32042. https://doi.org/10.1016/j.ceramint.2021.08.092.
30. Tsubota, T.; Ohtaki, M.; Eguchi, K.; Arai, H. Thermoelectric Properties of Al-Doped ZnO as a Promising Oxide Material for High-Temperature Thermoelectric Conversion. *J. Mater. Chem.* **1997**, *7* (1), 85–90. https://doi.org/10.1039/a602506d.
31. Nam, W. H.; Lim, Y. S.; Choi, S. M.; Seo, W. S.; Lee, J. Y. High-Temperature Charge Transport and Thermoelectric Properties of a Degenerately Al-Doped ZnO Nanocomposite. *J. Mater. Chem.* **2012**, *22* (29), 14633–14638. https://doi.org/10.1039/c2jm31763j.
32. Chen, D.; Zhao, Y.; Chen, Y.; Wang, B.; Chen, H.; Zhou, J.; Liang, Z. One-Step Chemical Synthesis of ZnO/Graphene Oxide Molecular Hybrids for High-Temperature Thermoelectric Applications. *ACS Appl. Mater. Interfaces* **2015**, *7* (5), 3224–3230. https://doi.org/10.1021/am507882f.
33. (12) Chen, H.; Sun, Q.; Tian, T.; Zheng, L.; Barré, M.; Monot-Laffez, I.; Makowska-Janusik, M.; Li, G.; Kassiba, A. H. Defects and Microstructure of Highly Conducting Al-Doped ZnO Ceramics Obtained via Spark Plasma Sintering. *J. Eur. Ceram. Soc.* **2020**, *40* (15), 5529–5534. https://doi.org/10.1016/j.jeurceramsoc.2020.06.030.
34. Tran Nguyen, N. H.; Nguyen, T. H.; Liu, Y. R.; Aminzare, M.; Pham, A. T. T.; Cho, S.;

Wong, D. P.; Chen, K. H.; Seetawan, T.; Pham, N. K.; Ta, H. K. T.; Tran, V. C.; Phan, T. B. Thermoelectric Properties of Indium and Gallium Dually Doped ZnO Thin Films. *ACS Appl. Mater. Interfaces* **2016**, *8* (49), 33916–33923. https://doi.org/10.1021/acsami.6b10591.

35. Nam, W. H.; Kim, B. B.; Seo, S. G.; Lim, Y. S.; Kim, J. Y.; Seo, W. S.; Choi, W. K.; Park, H. H.; Lee, J. Y. Structurally Nanocrystalline-Electrically Single Crystalline Zno-Reduced Graphene Oxide Composites. *Nano Lett.* **2014**, *14* (9), 5104–5109. https://doi.org/10.1021/nl5018089.
36. Nam, W. H.; Kim, B. B.; Lim, Y. S.; Seo, W. S.; Park, H. H.; Lee, J. Y.; Zhou, X. D. Enhanced Charge Transport in ZnO Nanocomposite Through Interface Control Using Multiwall Carbon Nanotubes. *J. Am. Ceram. Soc.* **2016**, *99* (6), 2077–2082. https://doi.org/10.1111/jace.14198.
37. Nam, W. H.; Kim, B. B.; Lim, Y. S.; Dae, K. S.; Seo, W. S.; Park, H. H.; Lee, J. Y. Phonon-Glass Electron-Crystals in ZnO-Multiwalled Carbon Nanotube Nanocomposites. *Nanoscale* **2017**, *9* (35), 12941–12948. https://doi.org/10.1039/c7nr03747c.
38. Park, K.; Seong, J. K.; Kwon, Y.; Nahm, S.; Cho, W. S. Influence of SnO2 Addition on the Thermoelectric Properties of Zn1 - XSnxO ($0.01 \leq x \leq 0.05$). *Materials Research Bulletin*. 2008, pp 54–61. https://doi.org/10.1016/j.materresbull.2007.02.018.
39. Jacob, J.; Rehman, U.; Mahmood, K.; Ali, A.; Mehboob, K.; Ashfaq, A.; Ikram, S.; Amin, N.; Hussain, S.; Ashraf, F. Improved Thermoelectric Performance of Al and Sn Doped ZnO Nano Particles by the Engineering of Secondary Phases. *Ceram. Int.* **2020**, *46* (10), 15013–15017. https://doi.org/10.1016/j.ceramint.2020.03.031.
40. Moriga, T.; Edwards, D. D.; Mason, T. O.; Palmer, G. B.; Poeppelmeier, K. R.; Schindler, J. L.; Kannewurf, C. R.; Nakabayashi, I. Phase Relationships and Physical Properties of Homologous Compounds in the Zinc Oxide-Indium Oxide System. *J. Am. Ceram. Soc.* **1998**, *81* (5), 1310–1316. https://doi.org/10.1111/j.1151-2916.1998.tb02483.x.
41. Hörlin, T.; Svensson, G.; Olsson, E. Extended Defect Structures in Zinc Oxide Doped with Iron and Indium. *J. Mater. Chem.* **1998**, *8* (11), 2465–2473. https://doi.org/10.1039/a805291c.
42. Hoemke, J., Tochigi, E., Tohei, T., Yoshida, H., Shibata, N., Ikuhara, Y., & Sakka, Y. (2018). Inversion domain network stabilization and spinel phase suppression in ZnO. *Journal of the American Ceramic Society*, *101*(6), 2616-2626.
43. Hoemke, J.; Khan, A. U.; Yoshida, H.; Mori, T.; Tochigi, E.; Shibata, N.; Ikuhara, Y.; Sakka, Y. Microstructural Analysis and Thermoelectric Properties of Sn-Al Co-Doped ZnO Ceramics. *AIP Conf.Proc.* **2016**, *1763*. https://doi.org/10.1063/1.4961357.
44. Jia, J.; Takasaki, A.; Oka, N.; Shigesato, Y. Experimental Observation on the Fermi Level Shift in Polycrystalline Al-Doped ZnO Films. *J. Appl. Phys.* **2012**, *112* (1). https://doi.org/10.1063/1.4733969.
45. Jain, A.; Sagar, P.; Mehra, R. M. Band Gap Widening and Narrowing in Moderately and Heavily Doped N-ZnO Films. *Solid. State. Electron.* **2006**, *50* (7–8), 1420–1424. https://doi.org/10.1016/j.sse.2006.07.001.
46. (46) Ferhat, M.; Zaoui, A.; Ahuja, R. Magnetism and Band Gap Narrowing in Cu-Doped ZnO. *Appl. Phys. Lett.* **2009**, *94* (14), 1–5. https://doi.org/10.1063/1.3112603.

47. Tsay, C. Y.; Cheng, H. C.; Tung, Y. T.; Tuan, W. H.; Lin, C. K. Effect of Sn-Doped on Microstructural and Optical Properties of ZnO Thin Films Deposited by Sol-Gel Method. *Thin Solid Films* **2008**, *517* (3), 1032–1036. https://doi.org/10.1016/j.tsf.2008.06.030.
48. Brochen, S.; Granier, C.; Feuillet, G.; Pernot, J. Role of Deep and Shallow Donor Levels on N-Type Conductivity of Hydrothermal ZnO. *Appl. Phys. Lett.* **2012**, *100* (5). https://doi.org/10.1063/1.3681168.
49. Wu, C.; Shen, L.; Yu, H.; Huang, Q.; Zhang, Y. C. Synthesis of Sn-Doped ZnO Nanorods and Their Photocatalytic Properties. *Mater. Res. Bull.* **2011**, *46* (7), 1107–1112. https://doi.org/10.1016/j.materresbull.2011.02.043.
50. Russo, V.; Ghidelli, M.; Gondoni, P.; Casari, C. S.; Li Bassi, A. Multi-Wavelength Raman Scattering of Nanostructured Al-Doped Zinc Oxide. *J. Appl. Phys.* **2014**, *115* (7). https://doi.org/10.1063/1.4866322.
51. Alim, K. A.; Fonoberov, V. A.; Shamsa, M.; Balandin, A. A. Micro-Raman Investigation of Optical Phonons in ZnO Nanocrystals. *J. Appl. Phys.* **2005**, *97* (12), 1–5. https://doi.org/10.1063/1.1944222.
52. Kranert, C.; Schmidt-Grund, R.; Grundmann, M. Surface- and Point-Defect-Related Raman Scattering in Wurtzite Semiconductors Excited above the Band Gap. *New J. Phys.* **2013**, *15*. https://doi.org/10.1088/1367-2630/15/11/113048.
53. Katiyar, R. S.; Dawson, P.; Hargreave, M. M.; Wilkinson, G. R. Dynamics of the Rutile Structure. III. Lattice Dynamics, Infrared and Raman Spectra of SnO2. *J. Phys. C Solid State Phys.* **1971**, *4* (15), 2421–2431. https://doi.org/10.1088/0022-3719/4/15/027.
54. a)Han, L.; Van Nong, N.; Zhang, W.; Hung, L. T.; Holgate, T.; Tashiro, K.; Ohtaki, M.; Pryds, N.; Linderoth, S. Effects of Morphology on the Thermoelectric Properties of Al-Doped ZnO. *RSC Adv.* **2014**, *4* (24), 12353–12361. https://doi.org/10.1039/c3ra47617k.b) Han, L.; Christensen, D. V.; Bhowmik, A.; Simonsen, S. B.; Hung, L. T.; Abdellahi, E.; Chen, Y. Z.; Nong, N. V.; Linderoth, S.; Pryds, N. Scandium-Doped Zinc Cadmium Oxide as a New Stable n-Type Oxide Thermoelectric Material. *J. Mater. Chem. A* **2016**, *4* (31), 12221–12231. https://doi.org/10.1039/c6ta03126a.
55. Zhang, D. B.; Zhang, B. P.; Ye, D. S.; Liu, Y. C.; Li, S. Enhanced Al/Ni Co-Doping and Power Factor in Textured ZnO Thermoelectric Ceramics Prepared by Hydrothermal Synthesis and Spark Plasma Sintering. *J. Alloys Compd.* **2016**, *656*, 784–792. https://doi.org/10.1016/j.jallcom.2015.10.062.
56. Zhang, D. B.; Li, H. Z.; Zhang, B. P.; Liang, D. D.; Xia, M. Hybrid-Structured ZnO Thermoelectric Materials with High Carrier Mobility and Reduced Thermal Conductivity. *RSC Adv.* **2017**, *7* (18), 10855–10864. https://doi.org/10.1039/c6ra28854e.
57. Prasad, R.; Bhame, S. D. Review on Texturization Effects in Thermoelectric Oxides. *Mater. Renew. Sustain. Energy* **2020**, *9* (1), 1–22. https://doi.org/10.1007/s40243-019-0163-y.
58. Baghdadi, N.; Salah, N.; Alshahrie, A.; Ansari, A. R.; Koumoto, K. The Effect of Morphological Modification on the Thermoelectric Properties of ZnO Nanomaterials. *Ceram. Int.* **2021**, *47* (5), 6169–6178. https://doi.org/10.1016/j.ceramint.2020.10.195.
59. Akshay, V. R.; Arun, B.; Suneesh, M. V.; Vasundhara, M. Surfactant-Induced Structural Phase Transitions and Enhanced Room Temperature Thermoelectric Performance in n-Type Bi2Te3 Nanostructures Synthesized via Chemical Route. *ACS Appl. Nano Mater.* **2018**, *1* (7), 3236–3250. https://doi.org/10.1021/acsanm.8b00464.
60. Akshay, V. R.; Suneesh, M. V.; Vasundhara, M. Tailoring Thermoelectric Properties

through Structure and Morphology in Chemically Synthesized N-Type Bismuth Telluride Nanostructures. *Inorg. Chem.* **2017**, *56* (11), 6264–6274. https://doi.org/10.1021/acs.inorgchem.7b00336.

61. Brockway, L.; Vasiraju, V.; Sunkara, M. K.; Vaddiraju, S. Engineering Efficient Thermoelectrics from Large-Scale Assemblies of Doped ZnO Nanowires: Nanoscale Effects and Resonant-Level Scattering. *ACS Appl. Mater. Interfaces* **2014**, *6* (17), 14923–14930. https://doi.org/10.1021/am5023489.
62. Nethravathi, C.; Rajamathi, C. R.; Rajamathi, M.; Maki, R.; Mori, T.; Golberg, D.; Bando, Y. Synthesis and Thermoelectric Behaviour of Copper Telluride Nanosheets. *J. Mater. Chem. A* **2014**, *2* (4), 985–990. https://doi.org/10.1039/c3ta12877f.
63. P. Wang, N. Chen, Z. Yin, F. Yang and C. Peng, *J. Cryst. Growth*, 2006, **290**, 56-60.
64. M. G. E. Guziewicz, T. Krajewski, Ł. Wachnicki, G. Łuka, W. Paszkowicz, J.Domagała, E. Przeździecka, E. Łusakowska, B. Witkowski, *Acta Phys. Pol. A*, 2009,**116**, 814-817.
65. N. Sadananda Kumar, K. V. Bangera and G. K. Shivakumar, *Semiconductors*, 2015, **49**,899-904
66. Gayner, C. Improved Electrical Conductivity and Thermoelectric Performance of ZnO by Doping with NaCl and CdO. *Chem. Eng. J.* **2021**, *413*, 128149. https://doi.org/10.1016/j.cej.2020.128149.
67. Liang, X. Recasting the Callaway and von Baeyer Thermal Conductivity Model on Defective Oxide Materials: The ZnO-In2O3 System as an Example. *Phys. Chem. Chem. Phys.* **2015**, *17* (41), 27889–27893. https://doi.org/10.1039/c5cp04999g.
68. (23) (24) Gonzalez-Julian, J.; Neuhaus, K.; Bernemann, M.; Pereira da Silva, J.; Laptev, A.; Bram, M.; Guillon, O. Unveiling the Mechanisms of Cold Sintering of ZnO at 250 °C by Varying Applied Stress and Characterizing Grain Boundaries by Kelvin Probe Force Microscopy. *Acta Mater.* **2018**, *144*, 116–128. https://doi.org/10.1016/j.actamat.2017.10.055.
69. Biswas, S.; Singh, S.; Singh, S.; Chattopadhyay, S.; De Silva, K. K. H.; Yoshimura, M.; Mitra, J.; Kamble, V. B. Selective Enhancement in Phonon Scattering Leads to a High Thermoelectric Figure-of-Merit in Graphene Oxide-Encapsulated ZnO Nanocomposites. *ACS Appl. Mater. Interfaces* **2021**, *13* (20), 23771–23786. https://doi.org/10.1021/acsami.1c04125.
70. a) An, D., Chen, S., Zhai, X., Yu, Y., Fan, W., Zhang, T., ... & Snyder, G. J. (2020). High-performance p-type elemental Te thermoelectric materials enabled by the synergy of carrier tuning and phonon engineering. *Journal of Materials Chemistry A*, *8*(24), 12156-12168. b)Chen, Z.; Ge, B.; Li, W.; Lin, S.; Shen, J.; Chang, Y.; Hanus, R.; Snyder, G. J.; Pei, Y. Vacancy-Induced Dislocations within Grains for High-Performance PbSe Thermoelectrics. *Nat. Commun.* **2017**, *8*, 1–8. https://doi.org/10.1038/ncomms13828.
71. Wu, Y.; Nan, P.; Chen, Z.; Zeng, Z.; Lin, S.; Zhang, X.; Dong, H.; Chen, Z.; Gu, H.; Li, W.; Chen, Y.; Ge, B.; Pei, Y. Manipulation of Band Degeneracy and Lattice Strain for Extraordinary PbTe Thermoelectrics. *Research* **2020**, *2020*, 1–12. https://doi.org/10.34133/2020/8151059.
72. Wu, Y.; Chen, Z.; Nan, P.; Xiong, F.; Lin, S.; Zhang, X.; Chen, Y.; Chen, L.; Ge, B.; Pei, Y. Lattice Strain Advances Thermoelectrics. *Joule* **2019**, *3* (5), 1276–1288. https://doi.org/10.1016/j.joule.2019.02.008.
73. Li, J.; Xie, Y.; Zhang, C.; Ma, K.; Liu, F.; Ao, W.; Li, Y.; Zhang, C. Stacking Fault-Induced Minimized Lattice Thermal Conductivity in the High-Performance GeTe-Based

Thermoelectric Materials upon Bi2Te3 Alloying. *ACS Appl. Mater. Interfaces* **2019**, *11* (22), 20064–20072. https://doi.org/10.1021/acsami.9b04984.

74. Yu, Y.; Zhou, C.; Zhang, S.; Zhu, M.; Wuttig, M.; Scheu, C.; Raabe, D.; Snyder, G. J.; Gault, B.; Cojocaru-Mirédin, O. Revealing Nano-Chemistry at Lattice Defects in Thermoelectric Materials Using Atom Probe Tomography. *Mater. Today* **2020**, *32* (February), 260–274. https://doi.org/10.1016/j.mattod.2019.11.010.
75. Liang, X. Thermoelectric Transport Properties of Naturally Nanostructured Ga-ZnO Ceramics: Effect of Point Defect and Interfaces. *J. Eur. Ceram. Soc.* **2016**, *36* (7), 1643–1650. https://doi.org/10.1016/j.jeurceramsoc.2016.02.017.
76. Liang, X.; Wang, C. Electron and Phonon Transport Anisotropy of ZnO at and above Room Temperature. *Appl. Phys. Lett.* **2020**, *116* (4). https://doi.org/10.1063/1.5139563.
77. Liang, X.; Yang, Y.; Dai, F.; Wang, C. Orientation Dependent Physical Transport Behavior and the Micro-Mechanical Response of ZnO Nanocomposites Induced by SWCNTs and Graphene: Importance of Intrinsic Anisotropy and Interfaces. *J. Mater. Chem. C* **2019**, *7* (5), 1208–1221. https://doi.org/10.1039/c8tc05148h.
78. Meng, X.; Liu, Z.; Cui, B.; Qin, D.; Geng, H.; Cai, W.; Fu, L.; He, J.; Ren, Z.; Sui, J. Grain Boundary Engineering for Achieving High Thermoelectric Performance in N-Type Skutterudites. *Adv. Energy Mater.* **2017**, *7* (13). https://doi.org/10.1002/aenm.201602582.
79. He, Y.; Lu, P.; Shi, X.; Xu, F.; Zhang, T.; Snyder, G. J.; Uher, C.; Chen, L. Ultrahigh Thermoelectric Performance in Mosaic Crystals. *Adv. Mater.* **2015**, *27* (24), 3639–3644. https://doi.org/10.1002/adma.201501030.
80. Althaf, R.; Ashok, A. M. Realization of High Thermoelectric Power Factor in Ta-Doped ZnO by Grain Boundary Engineering. *J. Appl. Phys.* **2020**, *128* (16), 0–13. https://doi.org/10.1063/5.0022287.
81. Guilmeau, E.; Díaz-Chao, P.; Lebedev, O. I.; Rečnik, A.; Schäfer, M. C.; Delorme, F.; Giovannelli, F.; Košir, M.; Bernik, S. Inversion Boundaries and Phonon Scattering in Ga:ZnO Thermoelectric Compounds. *Inorg. Chem.* **2017**, *56* (1), 480–487. https://doi.org/10.1021/acs.inorgchem.6b02354.(1)
82. Khan, A. U.; Kobayashi, K.; Tang, D. He, Y.; Lu, P.; Shi, X.; Xu, F.; Zhang, T.; Snyder, G. J.; Uher, C.; Chen, L. Ultrahigh Thermoelectric Performance in Mosaic Crystals. *Adv. Mater.* **2015**, *27* (24), 3639–3644. https://doi.org/10.1002/adma.201501030.
83. Park, Y. C.; Kim, Y. H.; Nahm, H. H.; Noh, J. Y.; Kim, Y. S.; Kim, J.; Lee, W. S.; Yang, J. M.; Park, J. Inversion Domain Boundaries on Tin (Sn)-Doped ZnO Nanobelts: Aberration-Corrected Scanning Transmission Electron Microscopy Study. *Appl. Phys. Lett.* **2013**, *102* (3). https://doi.org/10.1063/1.4788812.
84. Deng, R.; Zhang, X.; Zhang, E.; Liang, Y.; Liu, Z.; Xu, H.; Hark, S. Planar Defects in Sn-Doped Single-Crystal ZnO Nanobelts. *J. Phys. Chem. C* **2007**, *111* (35), 13013–13015. https://doi.org/10.1021/jp073668+.
85. Xin, J.; Wu, H.; Liu, X.; Zhu, T.; Yu, G.; Zhao, X. Mg Vacancy and Dislocation Strains as Strong Phonon Scatterers in Mg2Si1−xSbx Thermoelectric Materials. *Nano Energy* **2017**, *34* (January), 428–436. https://doi.org/10.1016/j.nanoen.2017.03.012.
86. Kim, S. Il; Lee, K. H.; Mun, H. A.; Kim, H. S.; Hwang, S. W.; Roh, J. W.; Yang, D. J.; Shin, W. H.; Li, X. S.; Lee, Y. H.; Snyder, G. J.; Kim, S. W. Dense Dislocation Arrays Embedded in Grain Boundaries for High-Performance Bulk Thermoelectrics. *Science*

(80-.). **2015**, *348* (6230), 109–114. https://doi.org/10.1126/science.aaa4166.
87. (5) Chen, Z.; Jian, Z.; Li, W.; Chang, Y.; Ge, B.; Hanus, R.; Yang, J.; Chen, Y.; Huang, M.; Snyder, G. J.; Pei, Y. Lattice Dislocations Enhancing Thermoelectric PbTe in Addition to Band Convergence. *Adv. Mater.* **2017**, *29* (23). https://doi.org/10.1002/adma.201606768.
88. (6) Hong, M.; Chen, Z. G.; Matsumura, S.; Zou, J. Nano-Scale Dislocations Induced by Self-Vacancy Engineering Yielding Extraordinary n-Type Thermoelectric Pb0.96-YInySe. *Nano Energy* **2018**, *50*, 785–793. https://doi.org/10.1016/j.nanoen.2018.06.030.
89. Daneu N, Rečnik A, Bernik S. Grain-growth phenomena in ZnO ceramics in the presence of inversion boundaries. J. Am. Ceram. Soc. 2011;94:1619–1626
90. Rečnik A, Daneu N, Walther T, et al. Structure and chemistry of basal-plane inversion boundaries in antimony oxide-doped zinc oxide. J. Am. Ceram. Soc. 2001;84:2657–2668
91. Rečnik A, Daneu N, Bernik S. Nucleation and growth of basal-plane inversion boundaries in ZnO. J. Eur. Ceram. Soc. 2007;27:1999–2008.
92. Giannozzi, P.; Baroni, S.; Bonini, N.; Calandra, M.; Car, R.; Cavazzoni, C.; Ceresoli, D.; Chiarotti, G. L.; Cococcioni, M.; Dabo, I.; Dal Corso, A.; De Gironcoli, S.; Fabris, S.; Fratesi, G.; Gebauer, R.; Gerstmann, U.; Gougoussis, C.; Kokalj, A.; Lazzeri, M.; Martin-Samos, L.; Marzari, N.; Mauri, F.; Mazzarello, R.; Paolini, S.; Pasquarello, A.; Paulatto, L.; Sbraccia, C.; Scandolo, S.; Sclauzero, G.; Seitsonen, A. P.; Smogunov, A.; Umari, P.; Wentzcovitch, R. M. QUANTUM ESPRESSO: A Modular and Open-Source Software Project for Quantum Simulations of Materials. J. Phys. Condens. Matter 2009, 21 (39). https://doi.org/10.1088/0953-8984/21/39/395502.
93. Yang, W.; Zhang, B.; Zhang, Q.; Wang, L.; Song, B.; Ding, Y.; Wong, C. P. Adjusting the Band Structure and Defects of ZnO Quantum Dots via Tin Doping. *RSC Adv.* **2017**, *7* (19), 11345–11354. https://doi.org/10.1039/c6ra25940e.
94. (109) Yin, J.; Lu, X. Theoretical Study Impurities Intermediate Band Material Based on Sn Heavily Doped ZnO by First Principles. *Superlattices Microstruct.* **2020**, *145* (December 2019), 106608. https://doi.org/10.1016/j.spmi.2020.106608.
95. Khuili, M.; El Hallani, G.; Fazouan, N.; El Makarim, H. A.; Atmani, E. H. First-Principles Calculation of (Al,Ga) Co-Doped ZnO. *Comput. Condens. Matter* **2019**, *21*, e00426. https://doi.org/10.1016/j.cocom.2019.e00426.
96. Xiong, Z.; Chen, L.; He, C.; Liang, Z. Ab Initio Studies of the Sn-Doped ZnO Transparent Conductive Oxide. *J. Phys. Conf. Ser.* **2011**, *276* (1). https://doi.org/10.1088/1742-6596/276/1/012194.
97. Imai, Y.; Watanabe, A. Comparison of Electronic Structures of Doped ZnO by Various Impurity Elements Calculated by a First-Principle Pseudopotential Method. *J. Mater. Sci. Mater. Electron.* **2004**, *15* (11), 743–749. https://doi.org/10.1023/B:JMSE.0000043423.16928.56.
98. Guan, W.; Zhang, L.; Wang, C.; Wang, Y. Theoretical and Experimental Investigations of the Thermoelectric Properties of Al-, Bi- and Sn-Doped ZnO. *Mater. Sci. Semicond. Process.* **2017**, *66* (February), 247–252. https://doi.org/10.1016/j.mssp.2017.03.027.
99. (1) Luo, Z. Z.; Hao, S.; Cai, S.; Bailey, T. P.; Tan, G.; Luo, Y.; Spanopoulos, I.; Uher, C.; Wolverton, C.; Dravid, V. P.; Yan, Q.; Kanatzidis, M. G. Enhancement of Thermoelectric Performance for N-Type PbS through Synergy of Gap State and Fermi

Level Pinning. *J. Am. Chem. Soc.* **2019**, *141* (15), 6403–6412. https://doi.org/10.1021/jacs.9b01889.

100. Park, K.; Choi, J. W.; Lee, C. W. Characteristics of Thermoelectric Power Modules Based on P-Type Na(Co0.95Ni0.05)2O4 and n-Type Zn0.99Sn0.01O. *J. Alloys Compd.* **2009**, *486* (1–2), 785–789. https://doi.org/10.1016/j.jallcom.2009.07.058.
101. Funahashi, R.; Matsumura, Y.; Urata, T.; Murakami, H.; Ikenishi, H.; Sasaki, S.; Sugiyama, S. Relationship Between Tensile Strength and Durability of Oxide Thermoelectric Modules. *J. Electron. Mater.* **2021**, *50* (7), 3996–4005. https://doi.org/10.1007/s11664-021-08934-4.
102. Rock, I. N. P.; Hong-kai, C.; Hong-mei, T. Í Ô) 1 , 2 ,. **2006**, *27* (2005), 967–974. **Mater. Res. Soc. Symp. Proc. Vol. 886 © 2006 Materials Research Society**
103. Funahashi, R.; Urata, S.; Mihara, T.; Nabeshima, N.; Iwasaki, K. Power Generation Using Oxide Thermoelectric Modules. *Ind. Ceram.* **2008**, *28* (3), 227–233. https://doi.org/10.4028/www.scientific.net/ast.46.158.
104. Souma, T.; Ohtaki, M.; Ohnishi, K.; Shigeno, M.; Ohba, Y.; Shimozaki, T. Power Generation Characteristics of Oxide Thermoelectric Modules Incorporating Nanostructured ZnO Sintered Materials. *Int. Conf. Thermoelectr. ICT, Proc.* **2007**, 38–41. https://doi.org/10.1109/ICT.2007.4569418.
105. Inagoya, A.; Sawaki, D.; Horiuchi, Y.; Urata, S.; Funahashi, R.; Terasaki, I. Thermoelectric Module Made of Perovskite Cobalt Oxides with Large Thermopower. *J. Appl. Phys.* **2011**, *110* (12). https://doi.org/10.1063/1.3671070.

Table 1. Comparison with other literature room temperature data of Electrical conductivity, Seebeck coefficient, carrier concentration, mobility, Effective mass, Fermi energy Doped ZnO.

Composition	σ (S/cm)	S (μVK^{-1})	n (cm^{-3})	μ ($cm^2V^{-1}S^{-1}$)	D.O.S (m^*/m_e)	Calculated Fermi energy (meV)	Ref
ZnO	13.97	-360	2.40E+18	3	0.29	0.0025	This work
2% Al Doped ZnO	130	-50	6.89E+19	13	0.332	0.184	31
2% Al Doped ZnO	315	-255	1.20E+18	10	0.28	0.0147	18
2% Al Doped ZnO	1300	-50.1	8.50E+19	50.7	0.58	0.121	56
2% Al Doped ZnO Rod //	490	-25	5.00E-01	45	0.43	0.115	5454
Rod ⊥	64	-25	2.53E+00	90	0.43	0.338	
platelet //	53	-25	3.08E+00	38	0.43	0.386	
platelet⊥	48	-25	2.34E+00	65	0.43	0.321	
Particle	25	-50	3.04E+00	8	0.38	0.382	
2% Al Doped ZnO	425	-9.60	3.54E+19	62	0.32	0.109	This work
1% Sn Doped ZnO	295	-115	1.62E+19	58	0.42	0.256	
Zn97Al2GaO100	543.48	-188	1.39E+20	53	0.9	0.108	61
Zn96Al2Ga2O100	429.18	-125	1.04E+20	55	0.41	0.196	
Zn96Al3GaO100	323.62	-113	6.00E+19	59	0.26	0.214	
Zn1−xCdxSc0.02O1.03 x = 0.05	177	−60.1	3.52 E+20	31.4	0.33	0.118	54
x = 0.15	193	−58.1	5.48 E+20	22.1	0.42	0.125	
2mol Al Doped ZnO - 1%RGO	1750	-40	2.40E+20	57	0.39	0.36	35
ZnO-2%RGO	2150	-38	7.00E+19	55.8	0.4	0.154	
2mol Al Doped ZnO 2%MWCNT	2500	-29	3.40E+20	46.5	0.38	0.466	36

$Zn_{0.97}Sn_{0.01}Al_{0.02}O$	225	-160	1.80E+20	57	0.72	0.136	This work
$Zn_{0.96}Sn_{0.02}Al_{0.02}O$	121	-170	1.42E+20	46	0.53	0.218	This work
$Zn_{0.95}Sn_{0.03}Al_{0.02}O$	24	-198	6.2E+19	33	0.47	0.118	This work